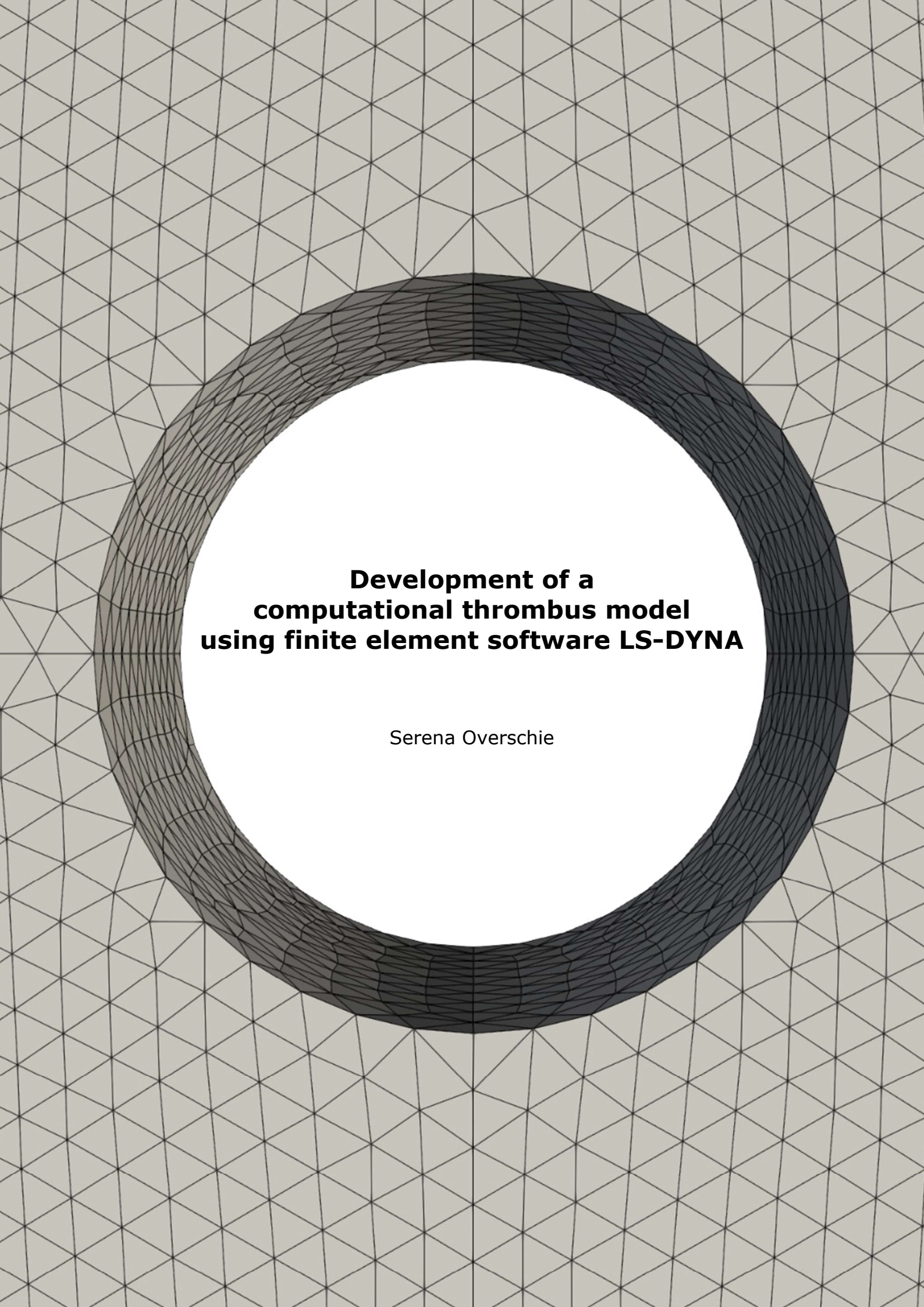

Development of a computational thrombus model using finite element software LS-DYNA

Serena Overschie

Development of a computational thrombus model using finite element software LS-DYNA

by

Serena Overschie

to obtain the degree of Master of Science in Biomedical Engineering at the Delft University of Technology, to be defended publicly on February 23th, 2022.

Student number: 4977408

Supervisors: Dr. ir. G. Luraghi
Dr. ir. F.J.H. Gijsen

Thesis committee: Dr. ir. G. Luraghi
Dr. ir. F.J.H. Gijsen
Dr. ir. M.J. Mirzaali Mazandarani

Technical University Delft – Erasmus University Medical Center

TU Delft

Erasmus MC
Universitair Medisch Centrum Rotterdam

Preface

An acute ischemic stroke is one of the leading causes of death and is caused by a thrombus that occludes a cerebral artery. This thrombus reduces the cerebral blood flow and causes irreversible brain tissue damage. Mechanical thrombectomy is a safe and effective technique to remove the thrombus from the cerebral arteries and restore the brain's blood flow. The mechanical properties of the thrombus highly influence the success rate of mechanical thrombectomy. To investigate the mechanical behavior of the thrombus under different loading conditions, numerical simulations could be performed. The aim of this thesis is to develop an in silico thrombus model to investigate the mechanical behavior of the thrombus under compressive and tensile loading conditions using finite element analysis software LS-DYNA. Experimental data collected from the lab is used to describe the mechanical behavior in the numerical thrombus models.

The building process of the in silico models in this study is organized in three parts. Part one is the cube model, where the material properties and numerical stable settings are investigated. Also, a combination of compression and tension is applied to the cube model to capture both the compressive and tensile forces present during mechanical thrombectomy. Part two includes geometry models that mimic the clot analog samples' geometry used during the experimental compression and tensile tests. Part three includes a clot analog with an initial hole in the middle to understand the fracture behavior of the thrombus. Different approaches to model fracture of the thrombus are investigated.

Three different parts characterize this thesis, and each includes a method, results, and discussion section. The discussion section of each part is dedicated to the decisions that have been made in that specific chapter. A discussion section is also included in the chapter Experiments. The general discussion at the end of this study will include the findings of each model and the comparison with literature. Recommendations for further research are given at the end.

In conclusion, this study provides a framework for modeling the thrombus under tensile and compressive loading, where the thrombus is modeled as a hyperelastic material. Future work is advised to extend and improve the models developed in this study.

Acknowledgments

As a member of the Biomechanics Laboratory Group at the Erasmus MC, I was allowed to perform my literature study "Interaction between thrombus and stent-retriever in acute ischemic stroke" followed by the thesis "Development of a numerical thrombus model using finite element software LS-DYNA" as presented in this document. I also got the opportunity to collaborate on the paper "In vitro and in silico modeling of endovascular stroke treatments for acute ischemic stroke" published in the Journal of Biomechanics in August 2021.

My last academic year would not have been the same without the support that I received. Therefore I would like to thank a few people. First of all, my supervisors Frank Gijsen and Giulia Luraghi. Thank you for the countless online meetings, sharing your knowledge and stimulating me to become 'a real engineer'. I am grateful for Suze-Anne, who always could fix my LS-DYNA-related problems. Thank you to Rachel Cahalane and Jo-anne Giezen for performing my experiments in the lab. Lastly, I would like to thank my master students from the Thrombus crew, Manouk, Emma, and Jo-anne. Without you guys my time in the lab would not be as fun and productive.

Last but not least, I would like to thank my parents, family, and friends who supported me along the way and celebrated the small and big victories with me.

This document contains my thesis to obtain the degree of Master of Science at the Delft University of Technology.

Serena C.M. Overschie
Naaldwijk, February 2022

Contents

1 Introduction

1.1 Acute ischemic stroke

An acute ischemic stroke is one of the leading causes of death and is caused by a thrombus that occludes a cerebral artery, as illustrated in figure 1.1 [1]. This thrombus reduces the cerebral blood flow and causes irreversible brain tissue damage [3]. A thrombus is generally formed to maintain the integrity of the vessel wall after injury [4]. The composition of thrombi is heterogeneous, where erythrocyte-rich and platelet-rich areas can be distinguished [3]. Histological research shows that the ratio of fibrin to red blood cell (RBC) content varies between thrombi [5]. Thrombi could contain up to 100% fibrin content and almost 80% RBC content [6]. The mechanical backbone of the thrombus is provided by the polymerization of fibrin, which results in a coarse, three-dimensional network of branching fibers. This mechanical backbone is mainly responsible for the thrombus's mechanical stability, shape, strength, and flexibility. The stiffness of the thrombus is influenced by the fiber thickness, fibers concentration, and branch point density [7][8].

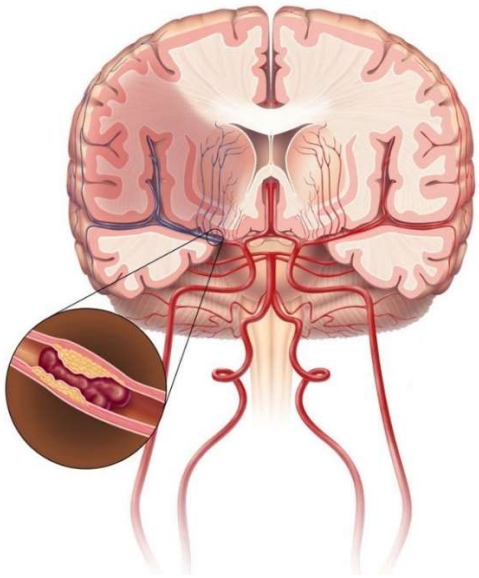

Figure 1.1: Illustration of a thrombus that occludes a cerebral artery and causes an acute ischemic stroke [2].

Removing the thrombus from the cerebral arteries is essential to restore the blood flow to the brain. If the patient arrives in the hospital within 4.5 hours of symptom onset, intravenous thrombolysis will be administered. This pharmacological treatment promotes fibrin degradation in the thrombus [9]. The solution for patients that arrived after 4.5 hours or showed resistance to intravenous thrombolysis came from clinical trials in 2015. These clinical trials showed that mechanical thrombectomy was a safe and effective technique [10]. The mechanical thrombectomy procedure can be performed with different techniques, including aspiration and the use of a stent-retriever [11].

1.2 Mechanical properties of the thrombus

Mechanical thrombectomy must be a fast and efficient process to remove a thrombus from the cerebral arteries. The retrieval forces must be greater than the resistance forces for successful removal. The resistance forces include the friction between the thrombus and vessel wall, the mechanical strength of the thrombus, and the hemodynamic stress caused by the blood flow. By applying a uniaxial tensile force during retrieval, the thrombus elongates and has the possibility to fracture due to hemodynamic forces and friction between the thrombus and vessel wall [12]. Understanding the mechanical properties of the thrombus is therefore of great importance to increase the chance of successful removal of the thrombus during mechanical thrombectomy.

Investigating the mechanical properties of thrombi retrieved with mechanical thrombectomy has some difficulties. These thrombi are already affected by the intravenous thrombolysis administered and exposed to excessive loading during mechanical thrombectomy. To perform reproducible experiments, homogeneous clot analogs can be made in vitro using animal or human blood [13]. Clot analog composition is related to the mechanical behavior of the thrombus, with fibrin rich clot analogs being stiffer compared to RBC rich clot analogs [14-15]. In vivo thrombi are viscoelastic materials with a non-linear stress-strain relationship [7].

1.3 Related work in silico studies

Performing in vitro studies to understand the mechanical behavior of the thrombus is very valuable. A different approach is using in silico studies that use numerical models. These numerical models are capable of studying the thrombus's mechanical properties and have potential on a larger scale. They can be used to speed up the development process, i.e., thrombectomy devices, because less animal and human testing are necessary [16]. A numerical thrombus model will be developed in this thesis.

Currently, the number of in silico studies investigating the mechanical behavior of the thrombus is scarce. There are multiple approaches to model the mechanical behavior of a thrombus, which can be in the solid or fluid domain [17]. The focus of this thesis will be placed on the solid domain. Up to this date, only a few papers developed an in silico model that includes a thrombus as a solid in one way or another. Numerical aspiration models modeled the thrombus as a cylinder, using an incompressible isotropic hyperelastic material [18-19] and an incompressible viscoelastic material [20] to describe the thrombus behavior. A total of three studies focused on the performance of a stent-retriever. One study modeled the thrombus as an incompressible hyperelastic solid material using the Mooney-Rivlin model [21]. Two studies modeled the thrombus as a compressible hyperelastic material, where a foam material was used with a Poisson's ratio of 0.3 [22-23]. The mechanical behavior under compressive loading was investigated by Johnson *et al.* using a near incompressible viscoelastic material [24]. They were capable of capturing the loading-unloading hysteresis and stress-relaxation of the thrombus. Tutwiler *et al*. developed a fibrin hydrogel with an initial crack to investigate the mechanical failure of fibrin [25]. The fibrin hydrogel was modeled as a biphasic material with the fibrous network as a solid mass filled with a liquid. Stretching of the fibrin hydrogel resulted in fiber alignment beyond and at the crack tip. Lastly, Fereidoonnezhad *et al.* developed an in silico model for thrombus fragmentation using an anisotropic hyperelastic material [26]. The Cohesive Zone Model was included in the numerical model to predict the fracture initiation and propagation of the clot analog. The fracture toughness increased with more fibrin rich clots.

1.4 Aim of the thesis

Different software programs are on the market for the two domains in which numerical thrombus models can be developed. The finite element method is frequently used for simulations in the solid domain, for example, with Abaqus [27]. On the contrary, computational fluid dynamics is usually solved with the finite volume method, for example, with Ansys Fluent [28]. An aspiration model is one of the applications where the fluid and solid domain combination is beneficial. Finite element analysis software LS-DYNA has the possibility to include this fluid-structure interaction [29]. LS-DYNA was created by the Livermore Software Technology Corporation and was acquired by Ansys in 2019. The aim of this thesis is to develop an in silico thrombus model to investigate the mechanical behavior of the thrombus under compressive and tensile loading conditions using finite element analysis software LS-DYNA. The thrombus will be modeled as a hyperelastic material in the solid domain, excluding the fluid domain. An explorative study will be deduced to learn the essential components of LS-DYNA and understand how the numerical models work without thoroughly investigating the details. Experimental data collected from the lab will be used to describe the mechanical behavior in the numerical thrombus models.

1.5 Outline of the thesis

This thesis consists of several chapters where the complexity of the thrombus model was gradually increased, and different options in LS-DYNA were investigated. First, the in vitro experiments are briefly explained, where compression and tensile tests are performed on two different clot analog compositions. These experiments were carried out by my colleagues at the Erasmus MC. Next, the numerical settings and different available material models in LS-DYNA are explained where suitable material models are selected. The building process of the in silico models of this thesis is organized in three parts. Part one is the cube model, which only contains one element, and therefore the mesh does not affect this model. Compression and tensile tests are performed to learn about the material models and assure numerical stability. Also, a combination of the compression and tensile test is applied to the cube model to capture both compressive and tensile forces present during mechanical thrombectomy. Part two includes geometry models that mimic the geometry of the samples used during the experimental compression and tensile tests. Part three includes a clot analog with an initial hole in the middle three to understand the fracture behavior of the thrombus. Different approaches to model fracture of the thrombus are investigated.

2 Experiments

In vitro tensile, fracture, and compression tests are performed on two different clot analog compositions. The experiments were carried out by my colleagues at the Erasmus MC, Rachel Cahalane (tensile test), and Jo-anne Giezen (compression test). They delivered the stress-strain curves and dimensions of the clot analogs. This chapter presents a short overview of how they made the clot analogs and performed the tensile, fracture, and compression tests. The last part describes the process of data selection and post-processing of the stress-strain curves.

2.1 Clot analogs

Most studies use bovine or ovine blood to investigate the mechanical behavior of the thrombus. Although the blood is histologically similar to that of human blood [13], this thesis uses human blood to make the clot analogs [30]. Tensile and compression tests were performed for two different clot compositions; platelet-rich plasma (PRP) and 40% RBC. Whole blood from different donor human subjects was used to make the clot analogs. Blood was collected in citrate plasma tubes and centrifuged to separate and take off the PRP and platelet-poor plasma. For both the 40% RBC and PRP sample, the PRP is added to the remaining solution of centrifuged blood together with $CaCl_2$ and thrombin. In addition to the 40% RBC sample, also the RBCs are added. After the solution is mixed, it is transferred to the molds (tensile and fracture test) and syringes (compression test). The samples need to overnight at 37 °C.

The clot analog molds for the tensile and fracture test are shown in figure 2.1. The shape and size of the molds are identical for both tests. The difference between the two molds is the inclusion of a rod. A rod is included in the mold used for the fracture test to ensure a 2 mm hole in the middle of the sample.

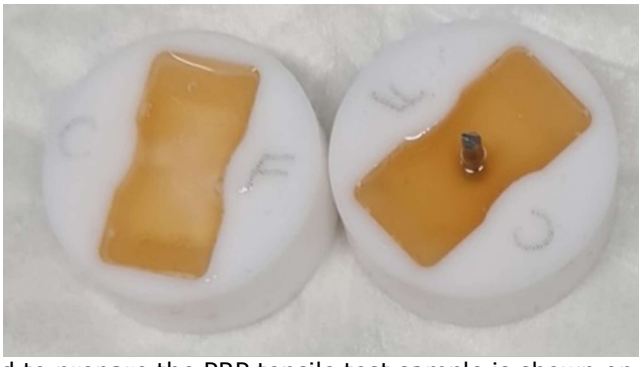

Figure 2.1: The mold used to prepare the PRP tensile test sample is shown on the left. On the right, the same mold includes a rod in the middle to ensure a 2 mm hole necessary for the fracture test samples. The shape and size of the molds used for the tensile and fracture test are identical.

The clot analog samples for the compression tests were made in a syringe. The top of the syringe was cut off, and the samples were removed using the stamper. They were placed in a container with Dulbecco's Modified Eagle Medium (DMEM), where the samples were cut from each clot composition with a height of 2 mm (figure 2.2). Before placing the samples on the stage of the compression tester in a 37 °C bath with DMEM solution, pictures were taken to define the dimensions later using ImageJ.

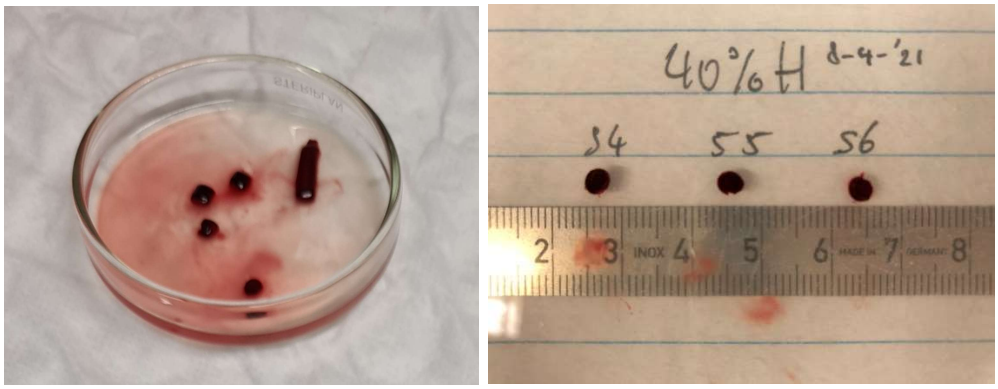

Figure 2.2: 40% RBC samples with a height of 2 mm were used for the compression test. On the left, the clot analog samples lay in a container with DMEM. On the right, the samples are placed on a piece of paper to determine the dimensions later using ImageJ.

2.2 Tensile test

The samples are removed from the molds and placed on the clamps, see figure 2.3. The clamps include double-sided foam tape and P400 sandpaper. The double-sided foam tape creates a two-layer bump to align the Velcro Tabs and distribute the stress. The top part of the clamps is attached by four screws using a torque screw.


Figure 2.3: Placement of the sample on the clamps of the tensile tester. Visible are the sandpaper, double-sided foam tape, and Velcro taps.

Rachel Cahalane performed the tensile experiments at the Erasmus MC. The settings for the preload and velocity were purely based on the expertise of Rachel Cahalane. A preload of 0.01 N was used for the PRP sample, whereas a preload of 0.005 N was used for the 40% RBC sample. The velocity was the same for both samples, 0.1 mm/s. This quasi-static velocity ensures that the inertial and viscoelastic effects can be neglected. Additional pictures of the specimen were collected to obtain the gauge length, width, and thickness using ImageJ.

2.3 Fracture test

The fracture test experiments are performed under uniaxial tensile loading. The same set-up and loading conditions described for the tensile test are used in the fracture tests. The goal of the fracture test is to investigate the strength of the clot analogs.

2.4 Compression test

The clot analog samples for the compression tests are placed in the 37 °C bath of the compression tester, with the set-up presented in figure 2.4. Jo-anne Giezen performed the compression experiments at the Erasmus MC. An 80% compression was applied for a total of 20 cycles, with a velocity of 0.2 mm/s.

Figure 2.4: Compression test set-up. The clot analog is placed in the 37 °C degrees DMEM bath. 80% compression for 20 cycles will be performed on the clot analog.

The fluid is pushed out of the clot analog during the 20 compression cycles in the compression test. As a result, the tissue changes. To describe the behavior of the clot analog, it is chosen to pick only the first loading curve of the stress-strain curve.

2.5 Data processing

Multiple data sets were compared in selecting appropriate data to be used in the numerical models. Much variation has been found between the different data sets, but the shape of the curves match. A curve in the middle is chosen to select a representative curve with all the variations present. For example, the curve from 4-6-2021 is selected for the tensile test using the PRP sample (figure 2.5). The different donors have not been taken into account. See Appendix A for all stress-strain curves.

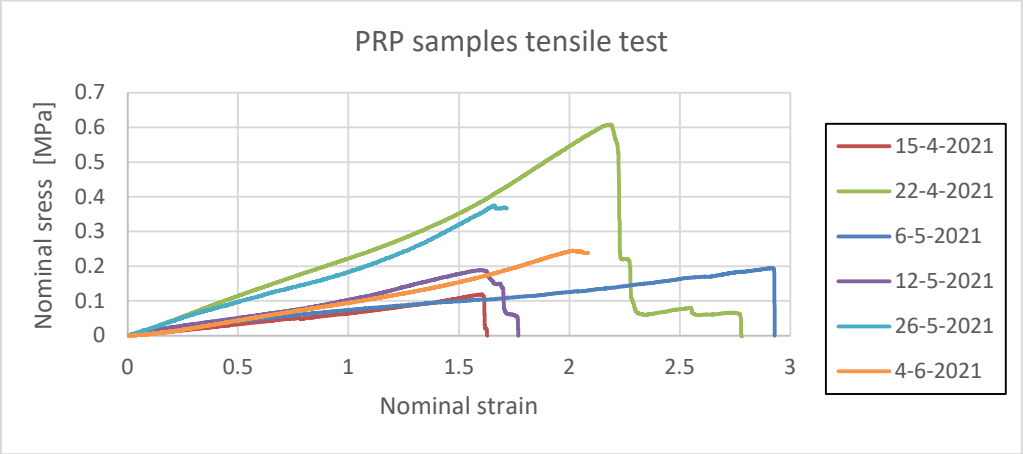

Figure 2.5: Stress-strain curves from all the tensile test experiments performed with the PRP samples. The PRP sample from 4-6-2021 is used for the tensile test.

A cubic spline filter is used to filter the data, and the negative stress values were removed. In Appendix B, the MATLAB code to filter the stress-strain curves is added.

The filtered curves used in the numerical models are shown in figure 2.6 for the PRP sample and figure 2.7 for the 40% RBC sample. Both figures include the stress-strain curves for the tensile, compression, and fracture tests. Each curve will be used in different parts of this thesis.

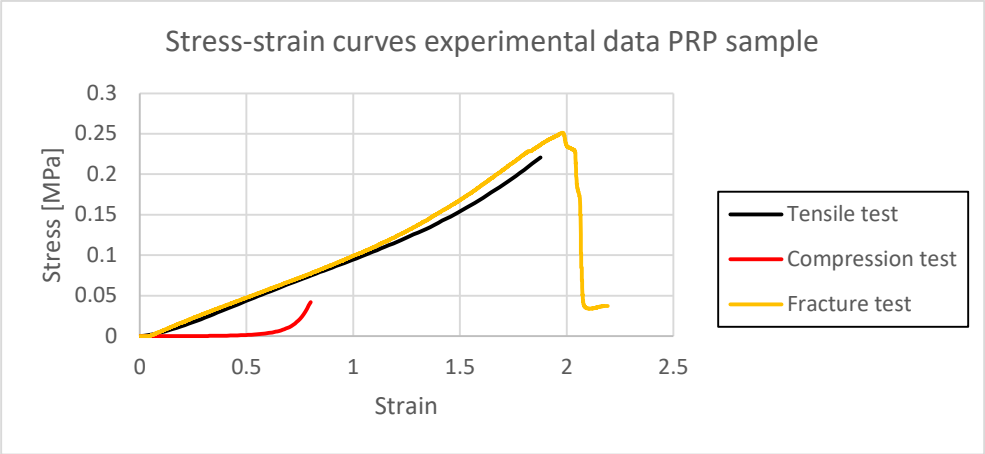

Figure 2.6: Stress-strain curves for the PRP sample. Included are the tensile test, compression test, and fracture test.

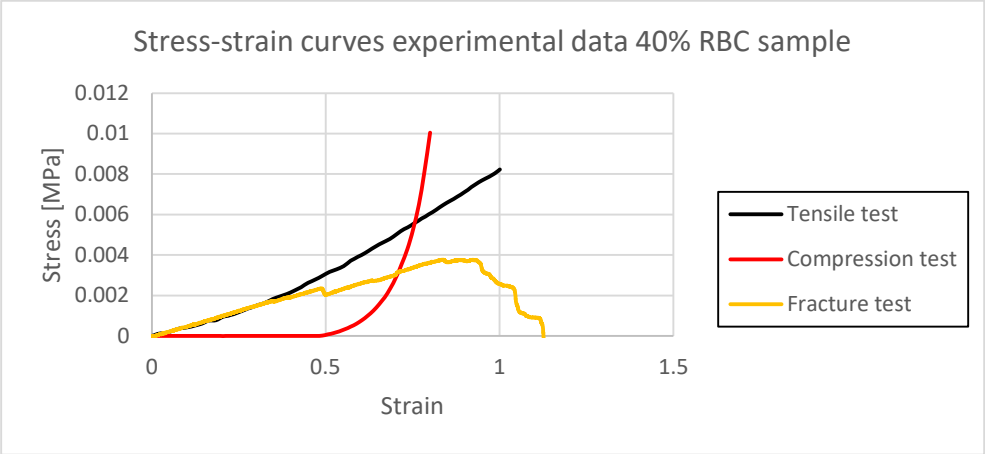

Figure 2.7: Stress-strain curves for the 40% RBC sample. Included are the tensile test, compression test, and fracture test.

2.6 Discussion

The experiments in this study were performed by my colleagues at the EMC. Some important decisions have been made to perform reproducible experiments, which influence the possibilities of the numerical models.

To understand the mechanical behavior of a thrombus with numerical models, experimental tests were performed on homogeneous clot analogs. These clot analogs made it possible to perform reproducible experiments. The numerical thrombus models developed in this thesis are homogeneous as well, which is consistent with previous studies that developed an in silico thrombus model [17-22][25-26][31]. It should be noted that a thrombus in vivo is heterogeneous, and this heterogeneity influences the thrombus (fracture) mechanics [3].

The clot analogs in this thesis were quasi-statically loaded, which ensures that the inertial and viscoelastic effects can be neglected. Therefore the property of viscoelasticity, which is present in the thrombus, is excluded in the models developed in this study [7].

The experimental tests were performed with two different clot compositions, but there were some problems with the 40% RBC sample during the tensile tests. The samples were very prone to fracture and therefore hard to handle during the tensile tests. Fracture occurred very often at the clamps. Better stress distribution would be beneficial for these softer materials. Sandpaper and foam tape were used to distribute the stress in the experiments, but this still did not give the desired result. One option to ensure non-uniform stress distribution in the samples is using a dogbone shaped sample. These samples have a larger cross-sectional area around the clamps, which reduces the stress at these locations. Failure of the sample will ultimately occur in the desired testing region [32].

3 Material models

Finite element analysis software LS-DYNA will be used to make numerical models of the clot analog samples. The mesh, boundary conditions, material properties, and solver options need to be defined to perform numerical simulations. The mesh, boundary conditions, and solver options are specific for each part of this thesis. For the specific settings used, see chapters 4 – 6. This chapter will briefly explain the material models that describe the material properties.

Material model 181 (MAT_SIMPLIFIED_RUBBER/FOAM) and material model 295 (MAT_ANISOTROPIC_HYPERELASTIC) were compared to each other. Both material models include compressibility and have one extra feature. This extra feature in material model 181 is the possibility to include a damage model. In material model 295, this extra feature is the possibility to add anisotropy.

3.1 Material model 181: Simplified rubber/foam

Material model 181 (MM181) is a phenomenological model that can be used for both rubber and foam materials. This material model is based on experimental observations, where curve-fitting is applied to the experimental test data [22][33]. The Poisson's ratio (PR) value determines whether the material model behaves as an incompressible rubber or compressible foam.

The compressible foam material is used for the numerical models built in this thesis. MM181 itself performs empirical curve fitting. The experimental stress-strain curve must be defined, and LS-DYNA fits the curve with a function. This function has the form of a classical Hill-Ogden strain energy potential for foams [22][33]. The stress response in the compressible foam material is formulated using the following equation:

$$\tau_{ij}^{E} = f(\lambda_i) - f\left(J^{-\frac{v}{1-2v}}\right), \tag{3.1}$$

with the principal Kirchhoff stresses denoted as τ_{ij}^{E}, the Poisson's ratio as v, principal stretches as λ_i, the ratio of the deformed to the undeformed state as J ($J = \lambda_1\lambda_2\lambda_3$), and f(.) the function determined directly from the uniaxial test data (compression and tension) and PR:

$$f(\lambda) = \lambda g(\lambda) + \lambda^{-v} g(\lambda^{-v}) + \ldots + \lambda^{(-v)^n} g\left(\lambda^{(-v)^n}\right), \tag{3.2}$$

with the experimental uniaxial curve defined as $\tau = g(\lambda)$.

Besides the stress-strain curve that must be defined, more parameters must be set for MM181. These parameters are the same for each simulation. The mass density has a value of 1 kg/dm^3, which corresponds with the value for blood and water [34]. The linear bulk modulus (KM) is calculated using the maximum derivative of the stress-strain curve. Different PRs are used to investigate which one is the best option to describe the behavior of the thrombus. The PR value for a solid thrombus model is not yet defined in the literature, and therefore a PR of 0.30, 0.35, 0.40, 0.45, and 0.49 is used. All other settings are set to the default settings.

3.2 Material model 295: Anisotropic hyperelastic

Material model 295 (MM295) is only available in version 12 of LS-DYNA. This hyperelastic material model contains different modules, including (in-)compressibility and (an)isotropy. MM295 is therefore useful for most biological soft tissues, including a thrombus. The Yeoh model can capture the non-linear behavior best, and therefore this empirical model will be used in the fitting procedure using a MATLAB script provided by Politecnico di Milano in Milan (Appendix C).

The Yeoh model is described by:

$$W = C_{10}(I_1 - 3) + C_{20}(I_1 - 3)^2 + C_{30}(I_1 - 3)^3, \tag{3.3}$$

with C10, C20, and C30 as material parameters and I_1 as the first invariant of the Cauchy-Green deformation tensor:

$$I_1 = \lambda_1^2 + \lambda_2^2 + \lambda_3^2, \tag{3.4}$$

where λ_i are the principal stretch values [35].

The MATLAB script only works for the compression test when the stress and strain values are negative. For the tensile and fracture test, these values must be positive.

Stress-strain curves obtained with the fitting procedure are presented in figure 3.1. These curves illustrate that the Yeoh model can fit the thrombus's non-linear behavior under tensile and compressive loading conditions.

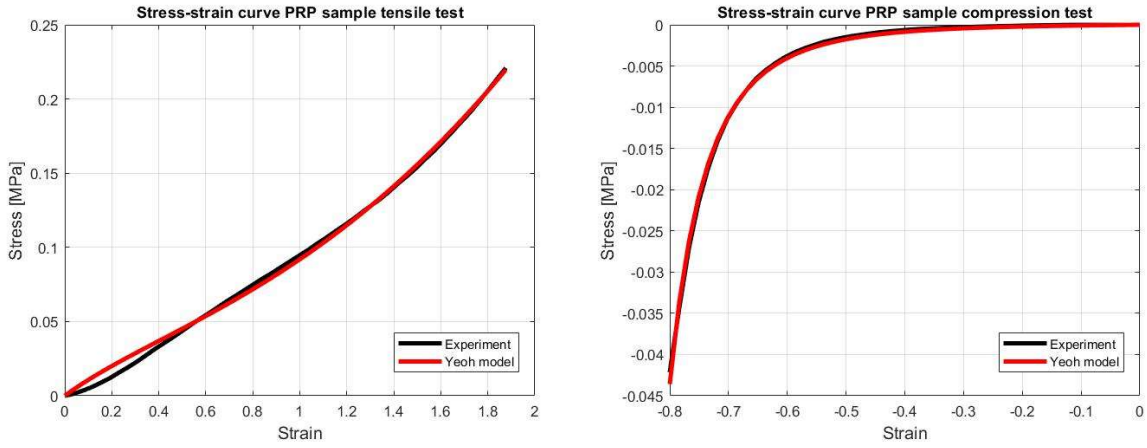

Figure 3.1: Stress-strain curves for the PRP sample for both the tensile test (left) and compression test (right). The Yeoh model is capable of describing the non-linear behavior of the thrombus.

After selecting the Yeoh model in MM295, the material parameters C10, C20, and C30 are included as C1, C2, and C3. Also, the mass density and PR must be defined. The mass density is again 1 kg/dm^3, and the PR within the range of 0.30 – 0.49 is tried to find the best fit. All other settings are set to the default settings.

The benefit of MM295 is the possibility of including anisotropy. However, the numerical models in this thesis do not include anisotropy.

4 Cube models

The cube model is the first step in the building process of the numerical thrombus model. This discretized with only one finite element cube model is made to ensure that the model works properly and to define the best choice for selecting the material properties without the interference of the mesh. First, the cube models' geometry, mesh, and boundary conditions are presented. Subsequently, the material parameters for the material models are presented. Next, the solver and post-processing procedure is described. Last, the cube model will be used to combine both compression and tension in one model. The choice of different numerical settings will be discussed in the discussion section. For a complete list of all the numerical keywords used for the cube model, the reader is referred to Appendix D.

4.1 Geometry, mesh, and boundary conditions

The cube model is discretized with only one hexahedron element, as illustrated in figure 4.1. Two types of boundary conditions were defined for the cube model. First, different translational constraints were applied on each node, as specified in table 4.1. Second, a boundary condition was defined for the application of tension or compression. A displacement in the y-translational direction is applied to the upper nodes of the cube (nodes 3, 4, 7, and 8) to accomplish tension and compression.

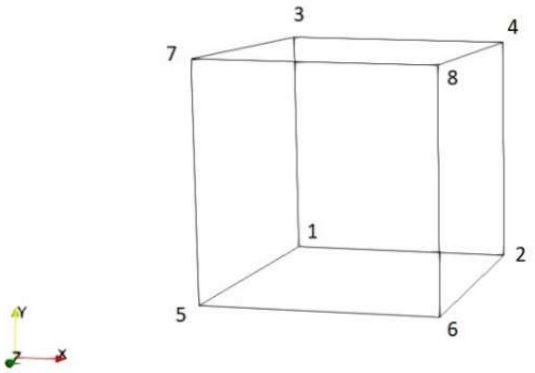

Figure 4.1: The cube model with the eight nodes specified.

Table 4.1. Overview of the coordinates in the x-, y-, and z-direction for each node and the constraints applied in each direction. An x denotes a constraint applied to that node in that specific direction.

Node	Coordinate			Constraint		
	x	y	z	x	y	z
1	0	0	0	x	x	x
2	1	0	0		x	x
3	0	1	0	x		x
4	1	1	0			x
5	0	0	1	x	x	
6	1	0	1		x	
7	0	1	1	x		
8	1	1	1			

4.2 Material models

MM181 and MM295 are both used in the cube models. The theory behind the material models is already discussed in chapter 3. The linear bulk modulus is an essential parameter in MM181. The used KM values for the cube models are found in table 4.2.
The Yeoh model is used to capture the non-linear behavior in MM295. The three material parameters (C10, C20, C30) received from the fitting procedure using equation 3.3 are shown in table 4.3.

Table 4.2. Linear bulk modulus (KM) values were calculated using the maximum derivative of the corresponding stress-strain curves.

Test	Composition	KM [MPa]
Tensile	PRP	0.20
	40% RBC	0.01
Compression	PRP	0.50
	40% RBC	0.20
Combination	PRP	0.50

Table 4.3. Material parameters that are found with the Yeoh model. These parameters are implemented in MM295 to describe the experimental curve.

Test	Composition	C10 [MPa]	C20 [MPa]	C30 [MPa]
Tensile	PRP	0.019419	0.001712	0
	40% RBC	0.001008	0.000360	0
Compression	PRP	0.000127	0.000049	0
	40% RBC	0.000043	0.000008	0

4.3 Solver

An explicit finite element solver without mass scaling is used for this quasi-static loading condition. Application of mass scaling is not necessary for this one element cube model because the computational time is already very low. For the cube models, a termination time of 100 ms is used. The timestep is set to the automatically calculated timestep by LS-DYNA. The scale factor for the computed time step is set to 0.8 to improve the stability of the model. The simulations were run using LS-DYNA R.12. on a Dell Precision 5820 Desktop with 32 GB RAM provided by Erasmus MC. Because the cube model only contains one element, the simulations are run with only 1 CPU.

4.3 Post-processing

To compare the numerical results with the experimental data, the nominal stress and strain of the cube model under tensile or compressive loading must be calculated. The outcome of the numerical simulations is the deformation tensor with principal components. The first and third principal stresses are used to calculate the nominal stress for respectively the tensile and compression test.

First, the three principal stretch values are calculated using the following equations:

$$\lambda_1 = e^{1P} \tag{4.1}$$
$$\lambda_2 = e^{2P} \tag{4.2}$$
$$\lambda_3 = e^{3PE} \tag{4.3}$$

with 1PE, 2PE, and 3PE, respectively being the first logarithmic principal strain, second principal strain, and third principal strain.

For the tensile test, the nominal strain and stress are calculated using the principal stretch values and the first principal stress value:

$$\varepsilon_n = (\lambda_1 - 1) \tag{4.4}$$

$$\sigma_n = \frac{1PS*(\lambda_1*\lambda_2*\lambda_3)}{\lambda_1} \tag{4.5}$$

with 1PS as the first principal stress.

For the compression test, the nominal strain and stress are calculated using the principal stretch values and the third principal stress value:

$$\varepsilon_n = (\lambda_3 - 1) \tag{4.6}$$

$$\sigma_n = \frac{3P\ *(\lambda_1*\lambda_2*\lambda_3)}{\lambda_3} \tag{4.7}$$

with 3PS as the third principal stress.

To quantify which PR gives the best fit with the experimental data, the difference in percentage at three different strain values is calculated between the numerical model and the experimental data using the following equation:

$$Error = \frac{\sigma_e - \sigma_n}{\sigma_e} * 100, \tag{4.8}$$

with σ_e as the experimental nominal stress and σ_n and the numerical nominal stress.

4.4 Results

Multiple simulations are performed to see which settings worked best for each material model and clot composition. To provide a clear overview of all the different results obtained from the cube model, the results are divided by test, clot analog composition, and material model. First, the results for the tensile test for both clot compositions are presented, starting with the PRP sample with both material models. After that, also the results of the compression test for both clot compositions are presented as well. The quality of the results was checked by looking at the ratio between the internal and kinematic energy (<5%), as well as the ratio between the internal energy and the dissipation energies (<10%) [36]. These ratios were acceptable for all cube models.

4.4.1 Tensile test PRP sample

The tensile test results for the PRP sample using MM181 are shown in figure 4.2. At low strain levels, each PR has a good fit with the experimental data. The curve using a PR of 0.49 differs from the other curves at large strain levels (table 4.4). The model using a PR of 0.30 best describes the mechanical behavior at both low and high strain levels.

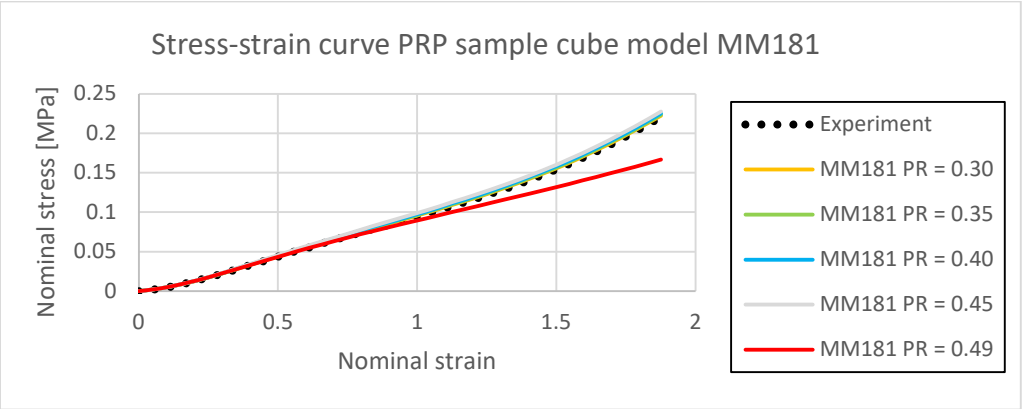

Figure 4.2: Stress-strain curve of the tensile test using the PRP sample and MM181. MM181 cannot capture the high strain behavior using a PR of 0.49.

Table 4.4. At three strain values (0.5, 1.0, and 1.5), the difference in percentage between PR and experimental data PRP sample and MM181 is calculated for the tensile test.

Strain	**Poisson's ratio**				
	0.30	0.35	0.40	0.45	0.49
0.5	3.3%	4.0%	5.1%	6.5%	2.4%
1.0	0.9%	1.6%	2.6%	4.1%	6.3%
1.5	1.6%	2.2%	3.1%	4.4%	16.3%

In contrast to MM181, a PR of 0.49 in MM295 with the PRP sample under tensile loading is best in describing the non-linear behavior of the thrombus at large strain levels (figure 4.3). The impact of the PR in MM295 is much larger than in MM181, where less non-linear behavior is found for low PR values (table 4.5). MM295 cannot capture the high strain behavior using low PR values.

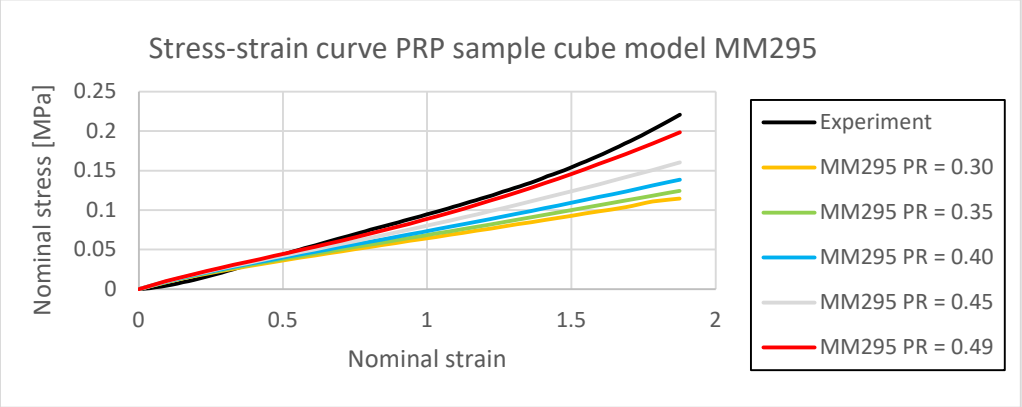

Figure 4.3: Stress-strain curve of the tensile test using the PRP sample and MM295. MM295 is only capable of capturing the non-linear behavior at high strains for a PR of 0.49.

Table 4.5. At three strain values (0.5, 1.0, and 1.5), the difference in percentage between PR and experimental data PRP sample and MM295 is calculated for the tensile test.

Strain	**Poisson's ratio**				
	0.30	0.35	0.40	0.45	0.49
0.5	14.1%	9.2%	3.9%	1.6%	6.4%
1.0	48.1%	39.4%	29.6%	18.1%	6.4%
1.5	64.8%	53.3%	40.0%	23.7%	5.0%

4.4.2 Tensile test 40% RBC sample

The tensile test results for the 40% RBC sample using MM181 are shown in figure 4.4. Contrary to the PRP sample, the stresses are much lower in the 40% RBC sample. At both low and high strains, all PRs can describe the non-linear behavior of the thrombus (table 4.6).

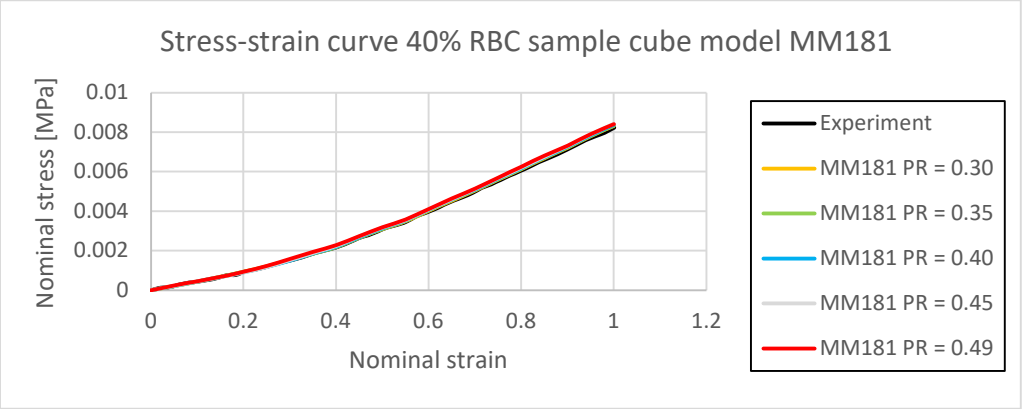

Figure 4.4: Stress-strain curve of the tensile test using the 40% RBC sample and MM181. All models with different PR can capture the mechanical behavior under tension.

Table 4.6. At three strain values (0.3, 0.5, and 0.8), the difference in percentage between PR and experimental data 40% sample and MM181 is calculated for the tensile test.

Strain	**Poisson's ratio**				
	0.30	0.35	0.40	0.45	0.49
0.3	0.9%	2.6%	3.3%	1.8%	2.4%
0.5	3.7%	3.8%	4.7%	5.4%	6.4%
0.8	1.8%	2.1%	2.3%	2.9%	3.8%

Similar behavior of MM295 as in the PRP sample is found for the 40% RBC sample (figure 4.5). The agreement between the numerical models and experimental data at low strain values is good, but at high strains it becomes less and less for the models with a PR in the range of 0.30 – 0.45. (table 4.7). MM295 can only capture the non-linear behavior at high strains with a PR of 0.49.

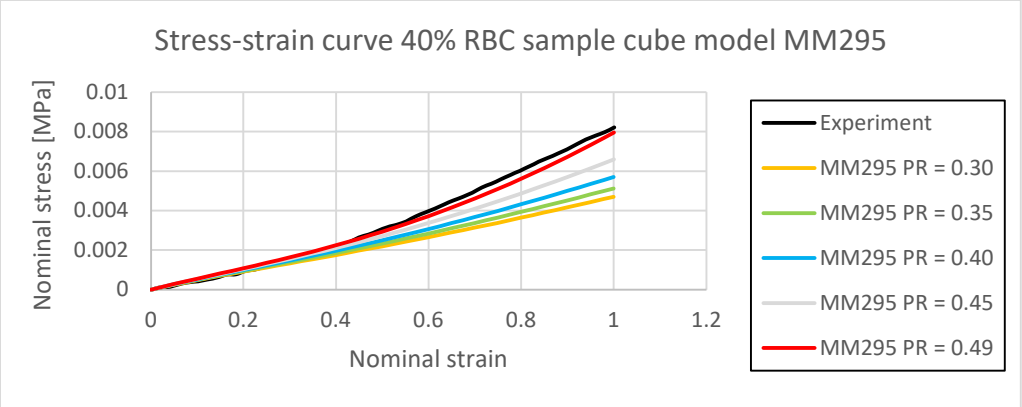

Figure 4.5: Stress-strain curve of the tensile test using the 40% RBC sample and MM295. MM295 cannot capture the non-linear behavior at high strains for low PR values.

Table 4.7. At three strain values (0.3, 0.5, and 0.8), the difference in percentage between PR and experimental data 40% sample and MM295 is calculated for the tensile test.

Strain	Poisson's ratio				
	0.30	0.35	0.40	0.45	0.49
0.3	15.5%	10.9%	5.4%	1.2%	6.0%
0.5	35.7%	27.5%	19.1%	9.7%	1.3%
0.8	65.2%	53.0%	39.0%	23.5%	7.0%

Looking at both the small and large deformations under tensile loading, MM181 with a PR of 0.30 and MM295 with a PR of 0.49 resulted in the best options to model the non-linear behavior of both clot compositions. The two curves are shown in figure 4.6 (PRP sample) and figure 4.7 (40% RBC sample). MM181 has a smaller difference with the experimental data for both clot compositions at each strain level than MM295 (table 4.8 and 4.9).

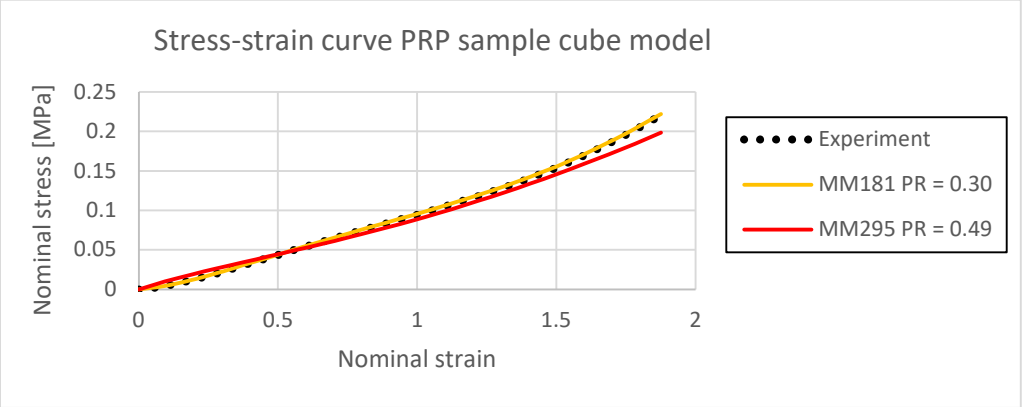

Figure 4.6: Stress-strain curve of the tensile test using the PRP sample and the best options for MM181 and MM295.

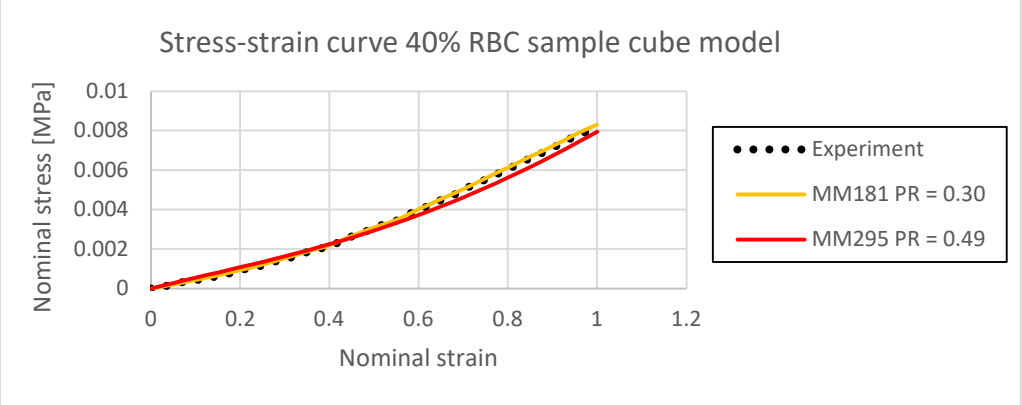

Figure 4.7: Stress-strain curve of the tensile test using the 40% RBC sample and the best options for MM181 and MM295.

Table 4.8. At three strain values (0.5, 1.0, and 1.5), the difference in percentage between the best options for MM181 and MM295 and the experimental data of the PRP sample for the tensile test is calculated.

Strain	PRP sample	
	MM181 PR = 0.30	MM295 PR = 0.49
0.5	3.3%	6.4%
1.0	0.9%	6.4%
1.5	1.6%	5.0%

Table 4.9. At three strain values (0.3, 0.5, and 0.8), the difference in percentage between the best options for MM181 and MM295 and the experimental data of the 40% RBC sample for the tensile test is calculated.

Strain	40% RBC sample	
	MM181 PR = 0.30	MM295 PR = 0.49
0.3	0.9%	6.0%
0.5	3.7%	1.3%
0.8	1.8%	7.0%

4.4.3 Compression test PRP sample

The compression test results for the PRP sample using MM181 are shown in two domains between 0.0 – 0.8 and from 0.0 – 0.5. The strain domain between 0.0 – 0.8 is shown in figure 4.8, and the strain domain of 0.0 – 0.5 in figure 4.9. MM181 has difficulties describing the non-linear behavior at high strains using a PR in the range of 0.40 – 0.49, where unreliable results were found (table 4.10). Using a PR of 0.30 and 0.35 on the other hand, a good comparison was found between the numerical models and the experimental data at these high strains. The numerical models had no problems describing the non-linear behavior in the low strain regions.

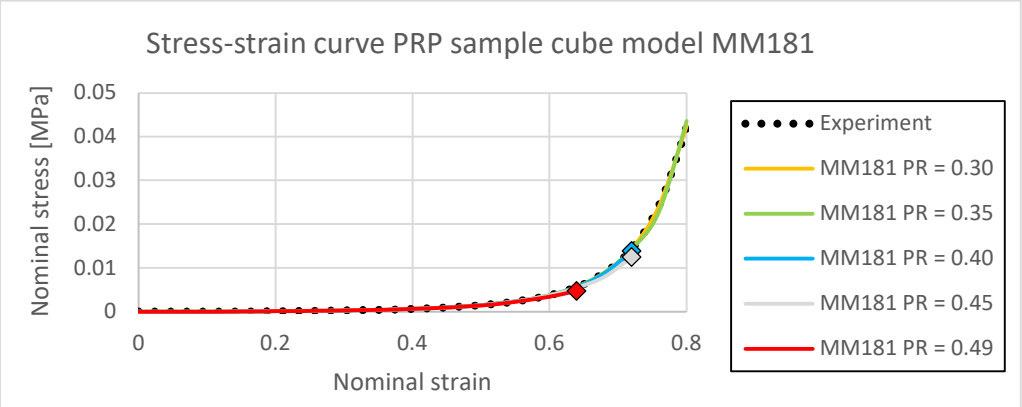

Figure 4.8: Stress-strain curve of the compression test using the PRP sample and MM181 with a strain domain between 0.0 and 0.8. Unreliable results are found after ◇.

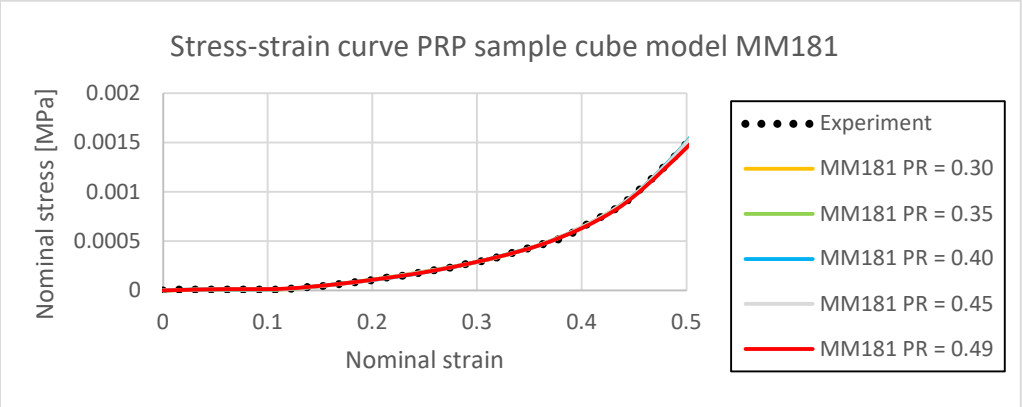

Figure 4.9: Stress-strain curve of the compression test using the PRP sample and MM181 with a strain domain between 0.0 and 0.5.

Table 4.10. At three strain values (0.3, 0.5, and 0.8), the difference in percentage between PR and experimental data PRP sample and MM181 is calculated for the compression test.

Strain	Poisson's ratio				
	0.30	0.35	0.40	0.45	0.49
0.3	8.0%	8.1%	8.9%	8.4%	8.8%
0.5	1.7%	1.9%	1.8%	2.5%	7.4%
0.8	0.7%	3.3%	107.2%	378431.7%	64.2%

The compression test results for the PRP sample using MM295 are again shown in two domains. First, the strain domain of 0.0 – 0.8 is shown in figure 4.10. Second, the strain domain of 0.0 – 0.5 in figure 4.11. For large compressive strain, MM295 can only describe the experimental data with a PR of 0.49. Considering the used numerical settings, all other PRs are unreliable for large deformations with differences >1000% (table 4.11).

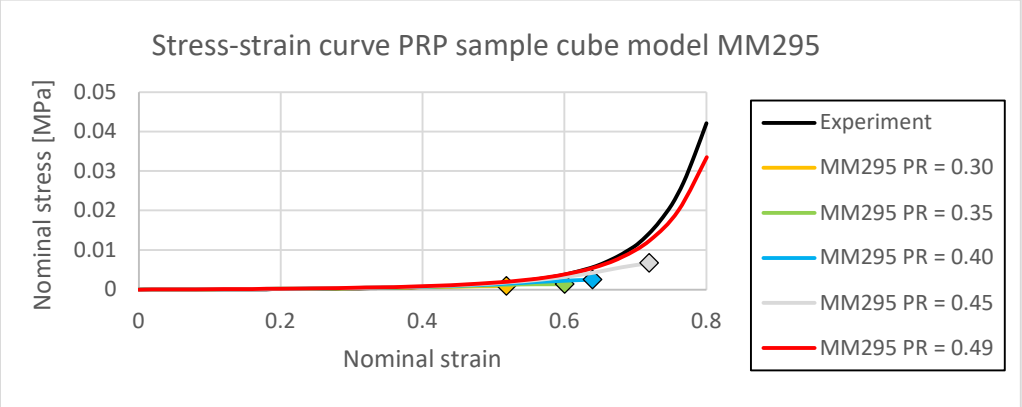

Figure 4.10: Stress-strain curve of the compression test using the PRP sample and MM295 with a strain domain between 0.0 and 0.8. Unreliable results are found after ◇.

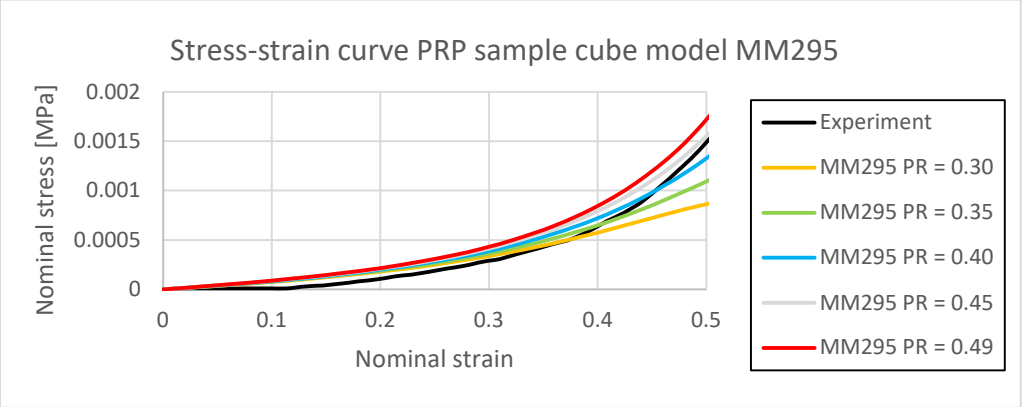

Figure 4.11: Stress-strain curve of the compression test using the PRP sample and MM295 with a strain domain between 0.0 and 0.5.

Table 4.11. At three strain values (0.3, 0.5, and 0.8), the difference in percentage between PR and experimental data PRP sample and MM295 is calculated for the compression test.

Strain	Poisson's ratio				
	0.30	0.35	0.40	0.45	0.49
0.3	17.3%	24.4%	28.6%	33.6%	37.2%
0.5	103.3%	53.0%	22.0%	1.8%	9.2%
0.8	39931.0%	30106.1%	19659.8%	5620.1%	25.7%

4.4.4 Compression test 40% RBC sample

The compression test results for the 40% RBC sample using MM181 are shown in figure 4.12. The stresses for the 40% RBC sample under compressive loading are much lower than the PRP sample, as seen in the tensile test. Corresponding with the PRP sample, MM181 finds it challenging to describe the non-linear behavior at high strains using a PR in the range of 0.40 – 0.49. Substantial differences are found between the numerical models and the experimental data (table 4.12).

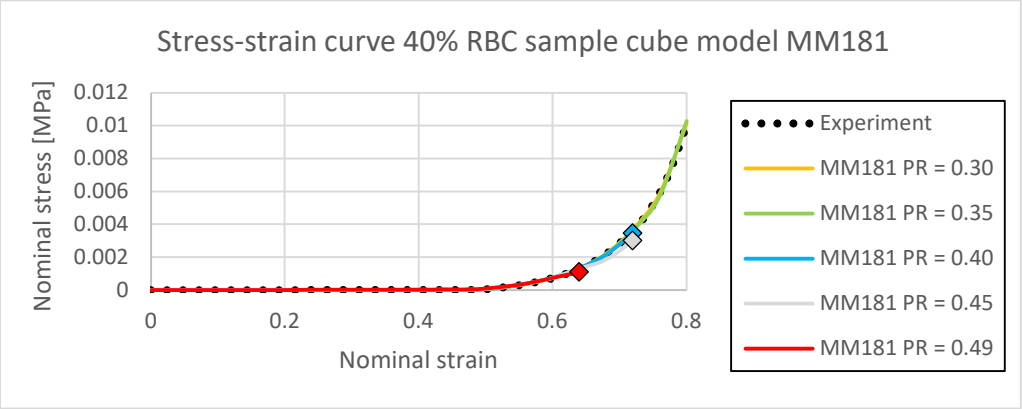

Figure 4.12: Stress-strain curve of the compression test using the 40% RBC sample and MM181 with a strain domain between 0.0 and 0.8. Unreliable results are found after ◇.

Table 4.12. At three strain values (0.3, 0.5, and 0.8), the difference in percentage between PR and experimental data 40% RBC sample and MM181 is calculated for the compression test.

Strain	**Poisson's ratio**				
	0.30	0.35	0.40	0.45	0.49
0.3	27.3%	29.4%	32.0%	35.1%	60.4%
0.5	45.3%	45.9%	46.6%	48.7%	54.4%
0.8	0.8%	2.2%	110.9%	4861.3%	3249.5%

The results for the compression test using the 40% RBC sample with MM295 are shown in figure 4.13. For large compressive strain, MM295 can only describe the experimental data with a PR of 0.49. This finding corresponds with the finding in the PRP sample. With the numerical settings used for this model, no reliable results are obtained at the high strain regions using a low PR (table 4.13).

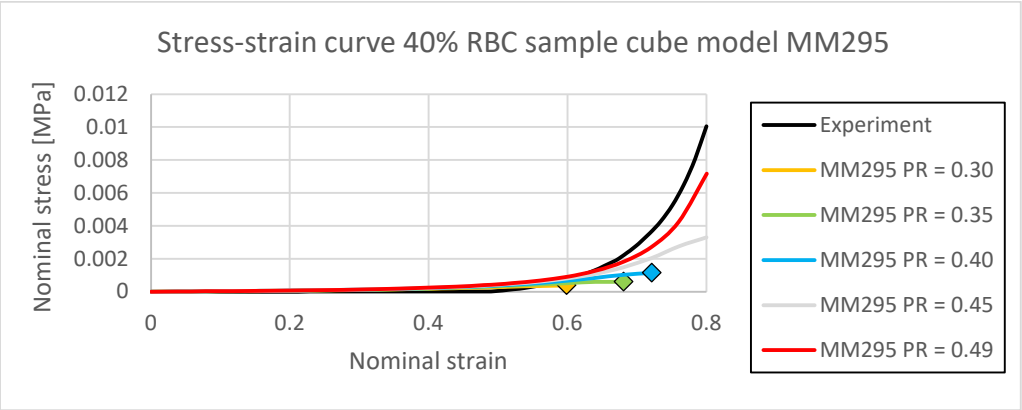

Figure 4.13: Stress-strain curve of the compression test using the 40% RBC sample and MM295 with a strain domain between 0.0 and 0.8. Unreliable results are found after ◇.

Table 4.13. At three strain values (0.3, 0.5, and 0.8), the difference in percentage between PR and experimental data 40% RBC sample and MM295 is calculated for the compression test.

Strain	Poisson's ratio				
	0.30	0.35	0.40	0.45	0.49
0.3	91.7%	92.0%	92.6%	93.0%	93.4%
0.5	74.0%	78.0%	81.0%	83.2%	84.4%
0.8	18120.1%	12258.0%	2702.3%	205.2%	40.2%

Looking at both the small and large deformations under compressive loading, MM181 with a PR of 0.30 and MM295 with a PR of 0.49 resulted in the best options to model the non-linear behavior of both clot compositions. The two curves are shown in figure 4.14 (PRP sample) and figure 4.15 (40% RBC sample). MM181 has a smaller difference with the experimental data for both clot compositions at each strain level compared to MM295 (table 4.14 and 4.15).

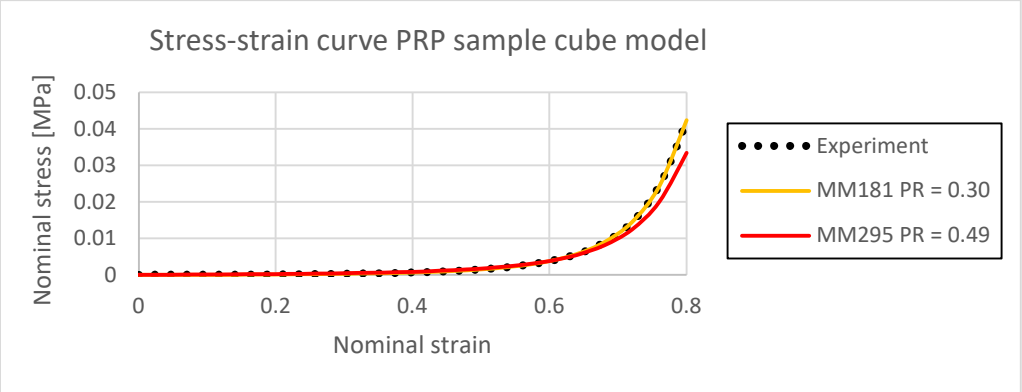

Figure 4.14: Stress-strain curve of the compression test using the PRP sample and the best options for both MM181 and MM295 with a strain domain between 0.0 and 0.8.

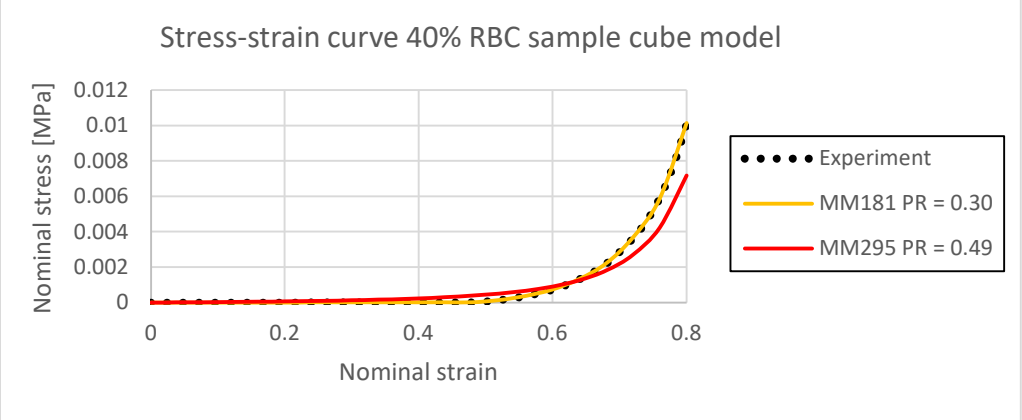

Figure 4.15: Stress-strain curve of the compression test using the 40% RBC sample and the best options for both MM181 and MM295 with a strain domain between 0.0 and 0.8.

Table 4.14. At three strain values (0.3, 0.5, and 0.8), the difference in percentage between the best options for MM181 and MM295 and the experimental data of the PRP sample for the compression test is calculated.

Strain	PRP sample	
	MM181 PR = 0.30	MM295 PR = 0.49
0.3	8.0%	37.2%
0.5	1.7%	9.2%
0.8	0.7%	25.7%

Table 4.15. At three strain values (0.3, 0.5, and 0.8), the difference in percentage between the best options for MM181 and MM295 and the experimental data of the 40% RBC sample for the compression test is calculated.

Strain	40% RBC sample	
	MM181 PR = 0.30	MM295 PR = 0.49
0.3	27.3%	93.4%
0.5	45.3%	84.4%
0.8	0.8%	40.2%

In conclusion, for MM181 a PR of 0.30 is the best option to describe the mechanical behavior of the clot analogs under both tensile and compressive loading conditions. For MM295, only a PR of 0.49 can describe the non-linear behavior during both tension and compression. Therefore, MM181 with a PR of 0.30 and MM295 with a PR of 0.49 will be used in the models developed in the next paragraph and the upcoming chapters of this thesis.

4.5 Combined tension and compression in one model

Both compressive and tensile forces are exposed to the thrombus during mechanical thrombectomy. In the models described in this paragraph, an attempt is made to combine both compression and tension in one model. As we know from previous experiments, the mechanical behavior of the thrombus is different under compressive and tensile loading conditions. That this poses new challenges is visible when MM295 is used. Empirical curve fitting using the Yeoh model with the stress-strain curve that combines compression and tension results in problems as illustrated in figure 4.16. For both the compression and tensile range, the Yeoh model cannot capture the behavior of the clot analog. Therefore it has been chosen not to continue with MM295 in this paragraph.

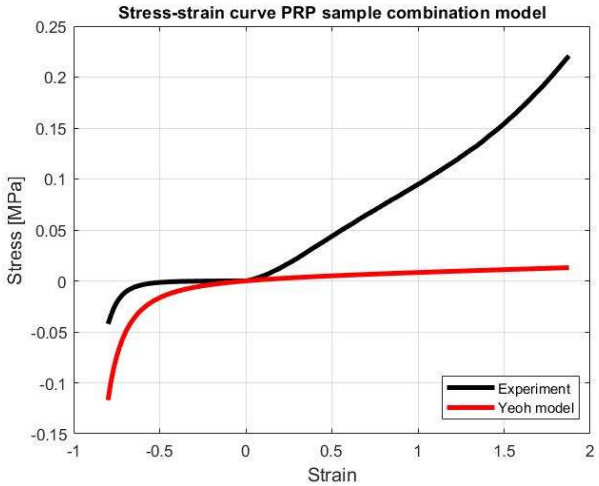

Figure 4.16: Stress-strain curve obtained after empirical curve fitting using the Yeoh model. The Yeoh model cannot describe the behavior of the clot analog under both compression and tensile loading conditions in one simulation.

The empirical curve fitting procedure is slightly different with MM181, as described in chapter 3.1. While combining tension and compression in one experiment, an asymmetric stress-strain curve is now implemented as input for MM181 with a PR of 0.3.

Two different simulations are performed on the cube model where tension and compression are combined to ensure that the model behaves the same regardless of the order of the loading conditions. One simulation where first tension is applied followed by compression (T-C test). Another simulation where first compression is applied followed by tension (C-T test). This simulation is in the opposite order compared with the T-C test.

4.6 Results

In figure 4.17, the stress-strain curve of the T-C test is shown. The stress-strain curve of the C-T test is presented in figure 4.18. To quantify the difference between the experimental data and the numerical models, the difference in percentage at four different strain values is displayed in table 4.16.

The stress-strain curves of both options have the same difference at a strain of -0.8 (2.8%) and -0.5 (8.7%). The compression range of the curve is thus similar at those specific strain levels. Minor differences are found for the tensile range. The difference at a strain of 0.5 is smaller for the C-T test than the T-C test. The same holds at a strain of 0.8, where the C-T test had a difference of 3.7% and the T-C test a difference of 4.0%. The differences between the T-C test and C-T test in the tensile range are minimal and within the numerical cut-off values.

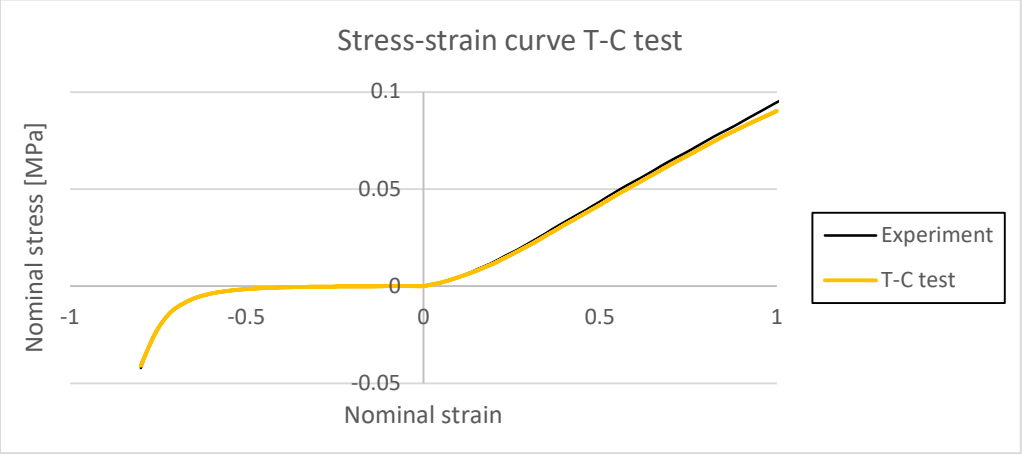

Figure 4.17: Stress-strain curve of the cube model where first tension is applied to the model, followed by compression.

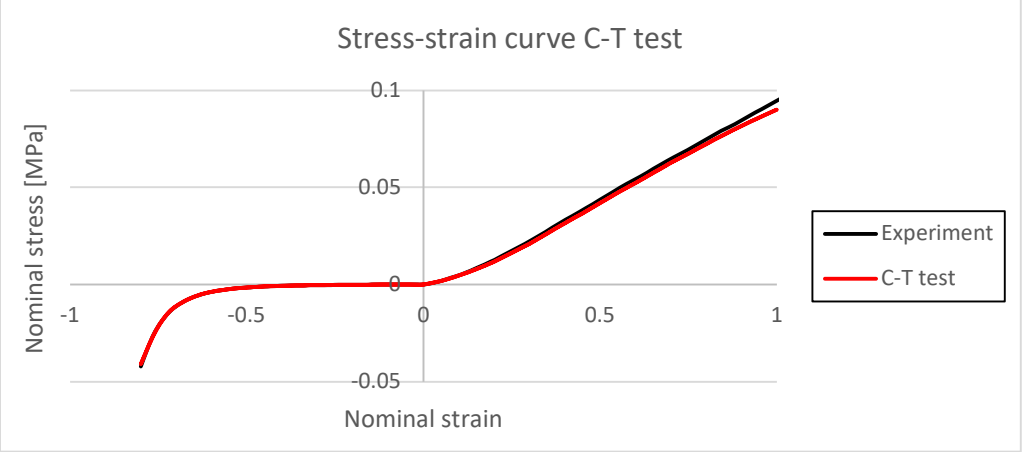

Figure 4.18: Stress-strain curve of the cube model where first compression is applied to the model, followed by tension.

Table 4.16. At four strain values (-0.8, -0.5, 0.5, and 0.8), the difference in percentage between the numerical models and experimental data is calculated. The minus sign denotes compression.

Strain	T-C test	C-T test
-0.8	2.8%	2.8%
-0.5	8.7%	8.7%
0.5	3.8%	3.5%
0.8	4.0%	3.7%

4.7 Discussion

The cube model is the starting point of the building process of the numerical thrombus model. To ensure that the model works properly and to define the best choice for selecting the material properties, several simulations were performed with different settings.

Several options and settings for keywords were investigated to get the numerical models up and running. Sensitivity analysis on different numerical parameters, i.e., timestep, termination time, damping, was performed to investigate the parameter's influence and get the correct value. It can be concluded that from this sensitivity analysis, it was not necessary to apply a very little timestep, increase the termination time or increase the damping. One parameter in MM181 seemed to significantly impact the results, namely the linear bulk modulus. This value must be derived from the maximum derivative of the stress-strain curve. The numerical results will become unstable when a too low value is used. It is therefore advised to round up the value of the maximum derivative.

Mass scaling was not implemented in the models used in this thesis. Applying mass scaling may help reduce the time needed in explicit solvers because the stable time increment is increased by increasing the mass. The downside of too much mass scaling is unwanted dynamic effects. Implementation of mass scaling did not have any benefits for the cube models, but it would have been in the geometry models. Therefore, adding this in more complex models is advised to reduce the computational time.

Both the implicit and explicit solver could have been used for all models developed in this study. The implicit solver is handy for models that contain only one part, which is the case for every model in this thesis. For the implicit solver, non-linear solution algorithms are required to calculate the next state. The computational cost is, therefore, very large. A thrombus is a non-linear material, and the future implementation of the thrombus model will be in a mechanical thrombectomy model. In these more complex models, multiple parts with additional contacts will be included [22]. These simulations require a lot more computational cost, and in that case, an explicit solver is advised. The new state can be directly calculated with the current state with the explicit solver. The computational cost is usually much smaller than for the implicit solver. For these reasons, it was decided to use the explicit solver for all the models in this study.

5 Geometry models

After finalizing the cube models where numerical stable settings were explored, the next step is to implement these settings into a geometry model. Due to the explorative nature of this thesis, the actual dimensions of the samples have not been used. An idealized geometry is used for both the compression and tensile models. Because these models contain way more elements, first, a mesh sensitivity analysis will be performed to ensure that the results are not affected by changing the element size of the mesh. After concluding the geometry and mesh, the boundary conditions of the geometry models are presented. Subsequently, the material parameters for the material models are presented. Apart from the number of processors used for the geometry model (4 CPUs), all other solver settings correspond with those used in the cube model in chapter 4. Therefore they will not be discussed in this chapter. Next, the post-processing procedure is described. The keywords used in the geometry models are similar to those of the cube models. Therefore, the reader is referred to Appendix E, where the two models' differences will be presented.

5.1 Geometry

The geometry of the tensile and compression test samples is made using SolidWorks2020. This exploratory thesis mainly focuses on the overall conclusions, and therefore a simplified geometry of both samples is used to describe the behavior of the thrombus under tension and compression. In the following two paragraphs, the specifications of both models are described.

5.1.1 Tensile test

The geometry model for both the PRP and 40% RBC sample differ. In figure 5.1 is on the left the PRP sample, and on the right the 40% RBC sample presented. The choice of the geometry for both samples is based on the gauge length, width, and thickness. As shown, the region within the orange box is used to define the geometry.

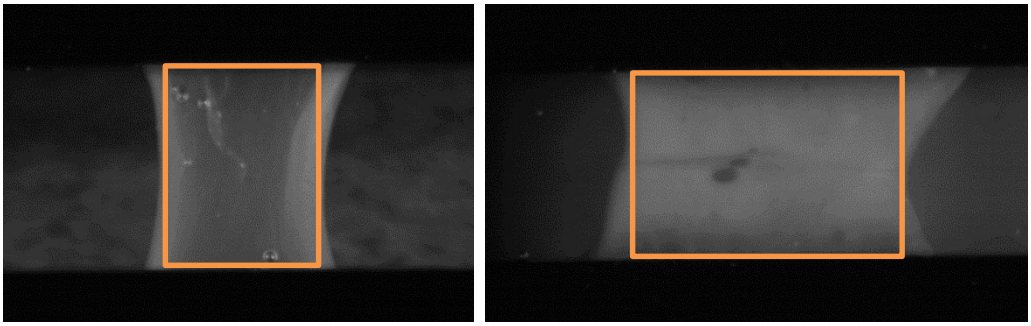

Figure 5.1: Images of the samples used during the tensile test. The PRP sample is on the left, and on the right is the 40% RBC sample. The area within the orange box is used to make the geometry models.

The dimensions of the rectangular shapes (gauge length, gauge width, and thickness) are presented in table 5.1, with a much larger thickness for the 40% RBC sample compared to the PRP sample. The initial cross-sectional area of the original sample is calculated using ultrasound images and is also presented in table 5.1. An illustration of the PRP and 40% RBC models are presented in figure 5.2.

Table 5.1. Dimensions used in the geometry models for the PRP and 40% RBC samples. The thickness of the 40% RBC is much larger compared to the PRP sample.

Sample	Gauge length [mm]	Gauge width [mm]	Thickness [mm]	Cross-sectional area [mm^2]
PRP	6.4	5.1	0.9	3.9
40% RBC	6.6	10.2	3.0	23.4

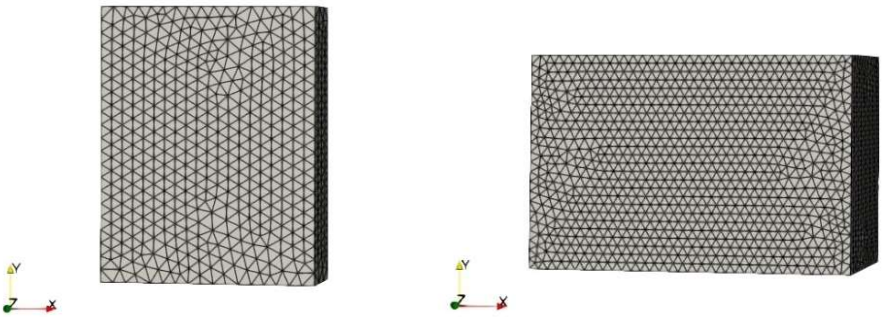

Figure 5.2: Tensile test geometries used for the PRP simulations (left) and 40% RBC simulations (right).

5.1.2 Compression test

The geometry model for both the PRP and 40% RBC samples slightly differs for the compression test. The choice of the geometry for both samples is based on the cross-sectional area, radius, and height. Although the shape is not cylindrical nor symmetrical in reality, it is chosen to make the model cylindrical and symmetrical based on the height and calculated radius.

The used dimensions for both samples are presented in table 5.2. An illustration of the PRP and 40% RBC models are presented in figure 5.3.

Table 5.2. Dimensions geometry models for the PRP and 40% RBC samples.

Sample	Radius [mm]	Height [mm]	Cross-sectional area [mm^2]
PRP	2.1	2.0	13.7
40% RBC	1.8	2.0	9.9

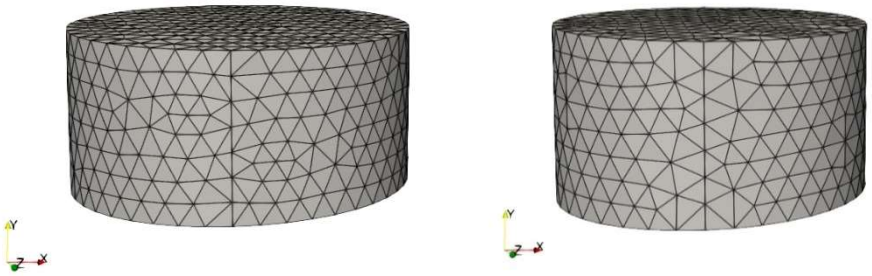

Figure 5.3: Compression test geometries used for the PRP simulations (left) and 40% RBC simulations (right).

5.2 Mesh

The clot analogs used in this thesis are modeled with a regular geometry. Looking at the future implementation, the clot analog will be modeled with an irregular complex shape based on in vivo geometries. The tetrahedral elements perform better in these irregular complex shapes than the hexahedral elements [36]. A mesh sensitivity analysis is performed to ensure that the results are not affected by changing the element size of the mesh. Different element sizes (0.2, 0.3, and 0.4 mm) of the tetrahedral mesh are investigated to see how many elements are required to ensure reliable results. The mesh sensitivity analysis is performed only on the PRP samples for the compression and tensile test using MM181 with a PR of 0.3 in all simulations. The simulations are run using Massage Passing Parallel (MPP) with 4 CPUs and 32 GB RAM.

A general comparison between the different element sizes of the tetrahedral mesh for both the tensile and compression test are presented in table 5.3. A non-linear decrease of the computational time has been observed for increasing element sizes.

Table 5.3. Comparison between different element sizes using the tetrahedral mesh for the tension and compression test.

Test	Element size [mm]	Number of elements	Number of nodes	Computational time [min]
Tensile	0.2	55911	10912	239
	0.3	14634	3099	39
	0.4	6573	1471	32
Compression	0.2	49687	9320	791
	0.3	13431	2668	191
	0.4	5597	1163	60

The nominal stress at two different timesteps is picked to quantify the differences between the different element sizes. The equation to calculate the error of the mesh in percentage from one mesh relative to another mesh is:

$$E_{i-j} = \frac{\sigma_i - \sigma_j}{\sigma_j} * 100, \tag{5.1}$$

with σ_i and σ_j as the nominal stress at the same timestep for the two different tetrahedral meshes.

Different graphs displaying the nominal stress and error between the meshes at timestep 20 and 36 for both the tensile and compression tests are shown in figure 5.4. The error values are presented in table 5.4.

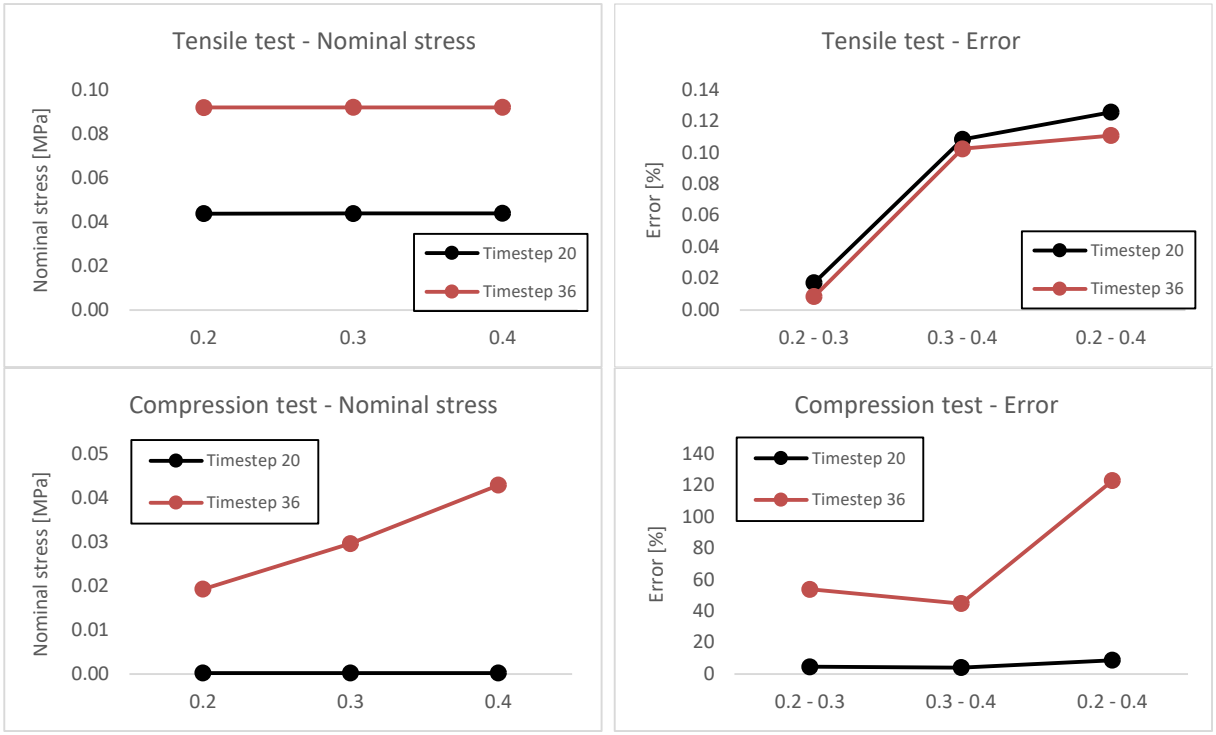

Figure 5.4: Quantitative analysis of the mesh sensitivity analysis for the tensile and compression test. The nominal stress at timestep 20 and 36 are shown on the left for all three mesh sizes. The error in percentage between the different meshes, as calculated with equation 5.1, is shown on the right.

Table 5.4. Quantitative analysis of the mesh sensitivity analysis for the tensile and compression test. Presented is the error between the different meshes for timestep 20 and 36. Substantial errors between the meshes are found for the compression test at timestep 36.

Test	Compared meshes	Timestep	Error (%)
Tensile	0.2 – 0.3	20	0.02
		36	0.01
	0.3 – 0.4	20	0.11
		36	0.10
	0.2 – 0.4	20	0.13
		36	0.11
Compression	0.2 – 0.3	20	4.55
		36	53.88
	0.3 – 0.4	20	4.13
		36	44.90
	0.2 – 0.4	20	8.87
		36	122.98

The maximum error for the tensile test between the 0.3 mm mesh and the finer mesh of 0.2 mm is <0.02%. This value is considered acceptable given the complexity of the geometry. The maximum error for the compression test between the 0.3 mm mesh and the finer mesh of 0.2 mm is <5% at timestep 20. This value is considered acceptable, and the elements' quality is good (figure 5.5). The error between the different meshes at timestep 36 is >40%. The mesh at timestep 36 is very deformed, and the quality of the elements is poor (figure 5.6).

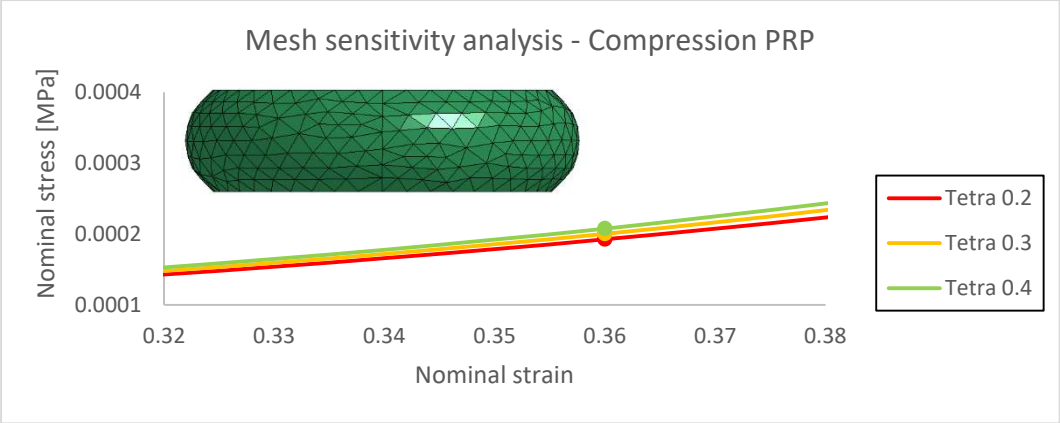

Figure 5.5: Mesh sensitivity analysis at timestep 20 corresponds with a strain of 0.36. The quality of the 0.3 mm tetrahedral elements is good at timestep 20.

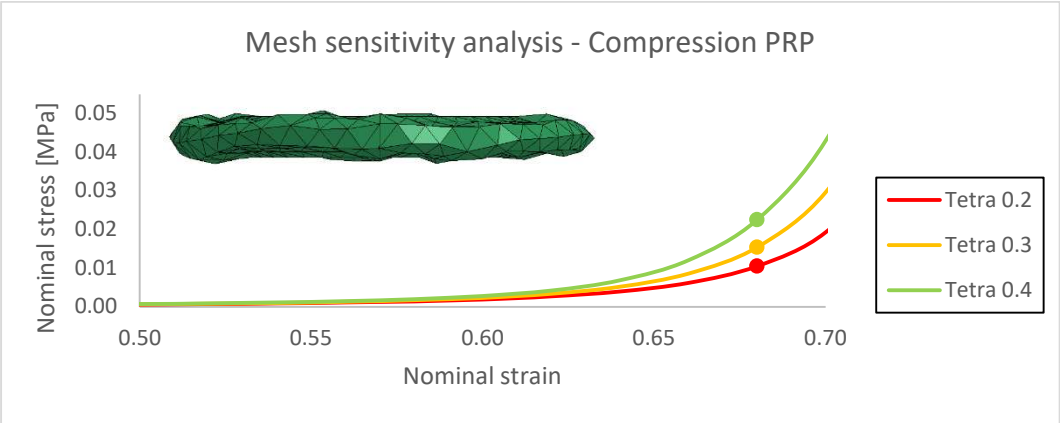

Figure 5.6: Mesh sensitivity analysis at timestep 36 corresponds with a strain of 0.68. The quality of the 0.3 mm tetrahedral elements is very poor at timestep 36.

To investigate the large error between the meshes and the poor quality of the elements at large deformations, simulations were performed with a finer mesh of 0.10 mm. This finer mesh shows that at high strains, it produces reliable looking outcomes (figure 5.7). For the computational cost reasons of this thesis, only one mesh is chosen which works fine for almost all simulations. Based on the error of the mesh, the computational time, and future implementation, it is chosen to continue with the tetrahedral mesh with an element size of 0.3 mm for both the compression and tensile test.

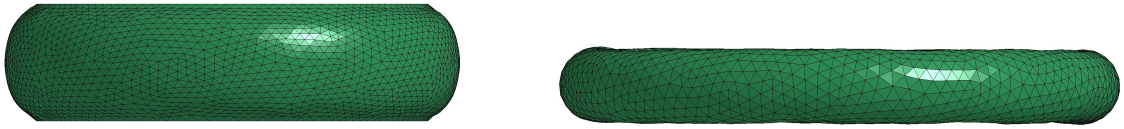

Figure 5.7: Mesh deformation at timestep 20 (left) and timestep 36 (right) with a mesh of 0.10 mm.

5.3 Boundary conditions

Two different node sets are made for the geometry model: the bottom and upper nodes. With these node sets, two types of boundary conditions were defined. First, the bottom nodes were fully fixed by constraining the translations and rotations in the x-, y-, and z-direction. The second boundary condition was defined for the application of tension or compression. A displacement in the y-translational direction is applied to the upper nodes of the model to accomplish tension and compression. The translations of the upper nodes in the x- and z-direction are fixed.

5.4 Material models

MM181 and MM295 are both used in the geometry models. The used KM values for the geometry models are shown in table 5.5 and implemented in MM181. The three material parameters (C10, C20, C30) received from the fitting procedure using equation 3.3 are presented in table 5.6. These values are implemented in MM295.

Table 5.5. Linear bulk modulus (KM) values were calculated using the maximum derivative of the corresponding stress-strain curves.

Type test	Composition	KM [MPa]
Tensile	PRP	0.20
	40% RBC	0.01
Compression	PRP	0.50
	40% RBC	0.20

Table 5.6. Material parameters that are found with the Yeoh model. These parameters are implemented in MM295 to describe the experimental curve.

Test	Composition	C10 [MPa]	C20 [MPa]	C30 [MPa]
Tensile	PRP	0.019419	0.001712	0
	40% RBC	0.001008	0.000360	0
Compression	PRP	0.000127	0.000049	0
	40% RBC	0.000043	0.000008	0

5.5 Post-processing

Because the geometry models contain way more elements than the one element cube model, it is not useful to execute the same procedure to calculate the nominal stress and strain values as described in chapter 4. For the geometry models, the resultant nodal force of the fixed bottom nodes is used to calculate the nominal stress and strain.

The displacement is calculated with:

$$\delta = t * v \tag{5.2}$$

with t as the time and v the velocity. The velocity is calculated with:

$$v = \frac{\delta_0}{t_0} \tag{5.3}$$

with δ_0 as the applied displacement and t_0 the time it takes to perform the displacement.

With the displacement and gauge length, the nominal strain can be calculated with the following equation for the tensile test:

$$\varepsilon_n = \frac{\delta}{L_0} \tag{5.4}$$

where L_0 is the gauge length.

For the compression test, the initial height of the clot analog will be used instead of the gauge length to calculate the nominal strain.

The nominal stress is obtained with:

$$\sigma_n = \frac{F}{A_0} \tag{5.5}$$

with F the resultant force of the fixed nodes and A_0 the initial cross-sectional area of the clot analog.

5.6 Results

Simulations are performed with MM181 (PR = 0.30) and MM295 (PR = 0.49) for the tensile and compression test for both clot analog compositions. To quantify the difference between the numerical models and the experimental data, the difference at three different strain values is calculated. The quasi-static hypothesis of the explicit simulations are confirmed for the geometry models.

5.6.1 Tensile test

The stress-strain curve for the PRP sample is shown in figure 5.8. Lower nominal stress values are achieved with the numerical models compared to the experimental data at both low and high strains, but MM181 and MM295 are identical in describing the behavior of the clot analog compared to the experimental data (table 5.7).

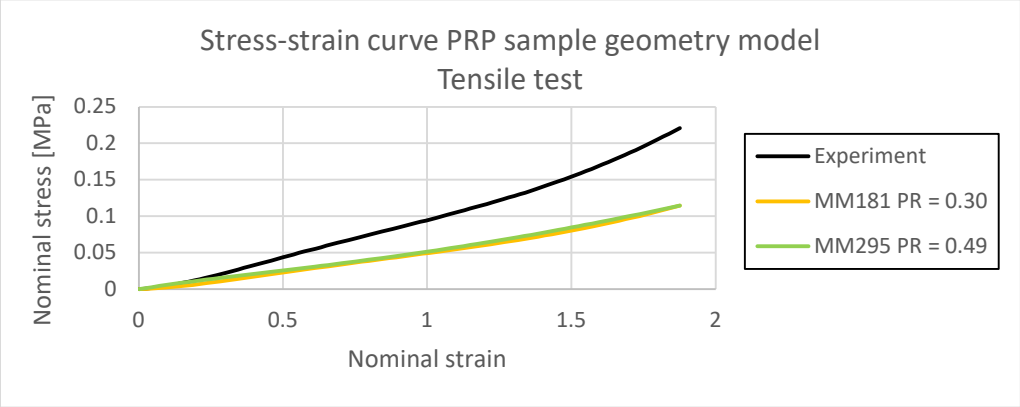

Figure 5.8: The stress-strain curve with the experimental tensile test data of the PRP sample and the numerical models with MM181 and MM295.

Table 5.7. At three strain values (0.5, 1.0, and 1.5), the difference in percentage between MM181 (PR = 0.30) and MM295 (PR = 0.49) and the experimental data of the PRP sample for the tensile test is calculated.

Strain	MM181 PR = 0.30	MM295 PR = 0.49
0.5	100.5%	80.2%
1.0	91.7%	83.6%
1.5	89.3%	80.5%

The stress-strain curve for the 40% RBC sample is shown in figure 5.9. Similar to the tensile test with the PRP sample, the same observations regarding the lower nominal stress achieved and the capability to model non-linearity apply for the 40% RBC sample (table 5.8).

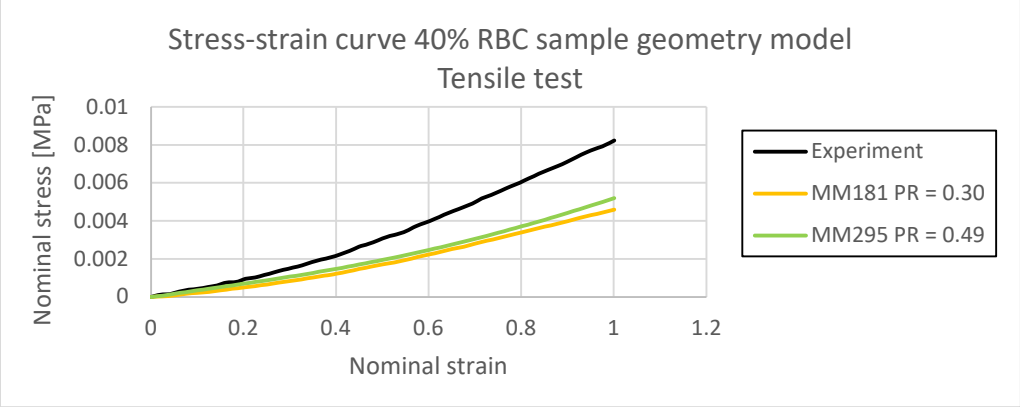

Figure 5.9: The stress-strain curve with the experimental tensile test data of the 40% RBC sample and the numerical models with MM181 and MM295.

Table 5.8. At three strain values (0.3, 0.5 and 0.8) the difference in percentage between MM181 (PR = 0.30) and MM295 (PR = 0.49) and the experimental data of the 40% RBC sample for the tensile test is calculated.

Strain	MM181 PR = 0.30	MM295 PR = 0.49
0.3	83.8%	44.4%
0.5	73.5%	53.1%
0.8	77.3%	62.1%

5.6.2 Compression test

The compression test results for the PRP sample are shown in two domains. First, the strain domain between 0.0 – 0.8 is shown in figure 5.10. Second, the strain domain of 0.0 – 0.6 is shown in figure 5.11. For large compressive strains, both MM181 and MM295 have problems describing the non-linear behavior (table 5.9). MM181 underestimates the nominal stress at low strain regions but overestimates the stress at high strain regions. The complete reverse applies to MM295.

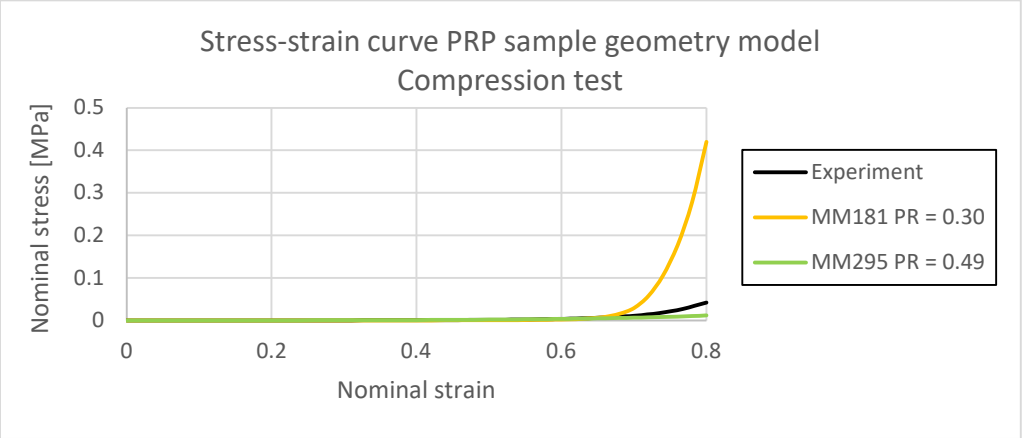

Figure 5.10: Stress-strain curve of the compression test using the PRP sample with a strain domain between 0.0 and 0.8.

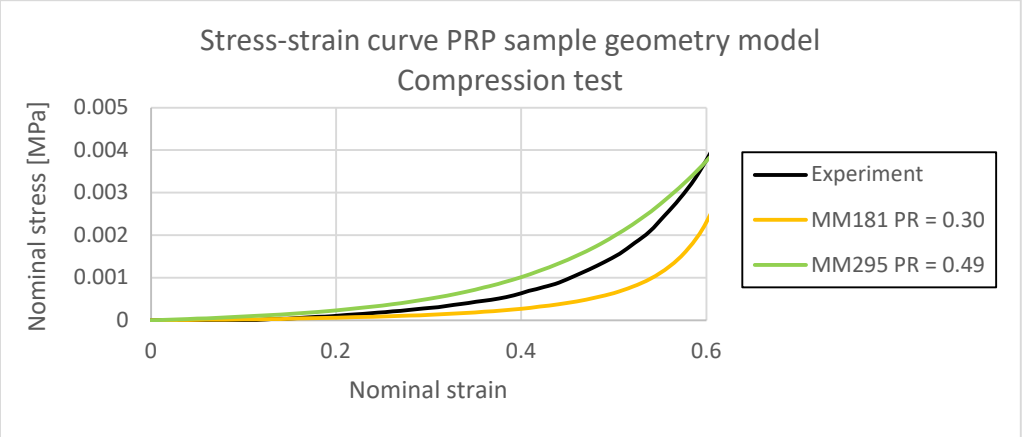

Figure 5.11: Stress-strain curve of the compression test using the PRP sample with a strain domain between 0.0 and 0.6.

Table 5.9. At three strain values (0.3, 0.5, and 0.8), the difference in percentage between MM181 (PR = 0.30) and MM295 (PR = 0.49) and the experimental data of the PRP sample for the compression test is calculated.

Strain	MM181 PR = 0.30	MM295 PR = 0.49
0.3	118.6%	44.6%
0.5	143.7%	20.6%
0.8	90.0%	257.5%

The stress-strain curve for the 40% RBC sample is shown in figure 5.12. Large differences are observed between the experimental data and the numerical models at each strain level (table 5.10). Both material models have problems describing the non-linear behavior at each strain level in the geometry model. MM181 has many problems describing the low strain behavior due to very low stress values, with differences >1000%.

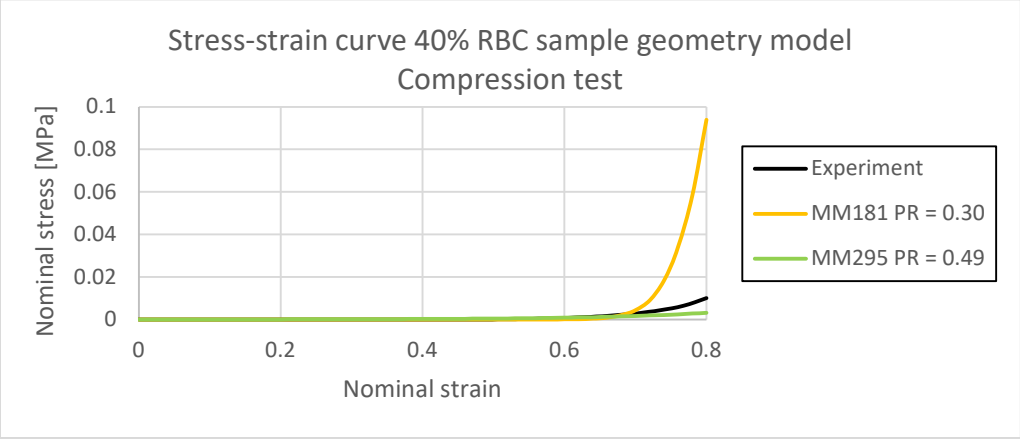

Figure 5.12: Stress-strain curve of the compression test using the 40% RBC sample with a strain domain between 0.0 and 0.8.

Table 5.10. At three strain values (0.3, 0.5, and 0.8), the difference in percentage between MM181 (PR = 0.30) and MM295 (PR = 0.49) and the experimental data of the 40% RBC sample for the compression test is calculated.

Strain	MM181 PR = 0.30	MM295 PR = 0.49
0.3	1991.7%	92.4%
0.5	584.4%	82.3%
0.8	89.3%	214.6%

5.7 Discussion

The geometry models were the next step in this thesis after concluding the cube models, where an idealized geometry was used. The models were meshed with tetrahedral elements, and simulations were performed with the best options for both material models with each clot composition.

With the combination of tetrahedral elements and a hyperelastic material, the mesh can highly deform without receiving an error. As a result, the error percentages between the different meshes for the compression test at timestep 36 exceeded 40%. In addition, the quality of the tetrahedral elements was not preserved at a high level of deformation. When interpreting the compression test results at high strains, it is essential to be careful. For future models, it is advised to pay attention to the dimension of the elements in the compression test.

A difference in nominal stress has been observed between the numerical models and the experimental data. Recalling the good comparison between the experimental data and the two numerical models in the cube model, this discrepancy in the geometry model could be linked to the geometry. The geometry used in the numerical models is different from the geometry of the experimental samples.

6 Fracture models

Thrombus fracture mechanics occur in several phases of the mechanical thrombectomy procedure, with the risk of downstream embolism. Therefore the last part of this thesis includes models where fracture is applied. Experimental tests are performed on samples with an initial hole in the middle for both clot analog compositions. An idealized geometry is used to mimic the actual dimensions of the samples used in these experiments. First, the mesh sensitivity analysis will be performed to ensure that the results are not affected by changing the element size of the mesh. Apart from the material parameters, the numerical settings for the models correspond with those used in chapter 5 and will not be discussed in this chapter. In three different parts, the building process of the fracture model is presented. To clearly distinguish the three different parts, the concepts of fracture, failure, and damage are introduced. In the context of this study, failure and fracture are the same, namely complete rupture of the clot analog. Damage refers to the evolution of a possible crack before fracture. In part one, numerical simulations are performed without including fracture to determine the strength of the clot analogs using experimental data. In part two, material failure is modeled using a critical value at which the clot analog will fracture abruptly. Material failure has been performed with both material models. Part three is dedicated to the damage model present in MM181, where a general failure criterion is used to model damage evolution before fracture. The quasi-static hypothesis of the explicit simulations is confirmed for all models in this chapter.

6.1 Geometry

The geometry of the fracture test samples is made using SolidWorks2020. Similar to the geometry models used in chapter 5, the geometry of the fracture models is also not an exact replication of the samples used during the experiments. The fracture tests are performed using a uniaxial tensile tester on clot analog samples with an initial hole of 2 mm in the middle. The choice of the geometry for both samples is based on the gauge length, width, and thickness. An illustration of the PRP and 40% RBC model is presented in figure 6.1, where the contribution of the hole in the PRP sample is much larger than the 40% RBC sample. The used dimensions for both samples are presented in table 6.1.

Table 6.1. Dimensions of the fracture models for the PRP and 40% RBC samples.

Sample	Gauge length [mm]	Gauge width [mm]	Thickness [mm]	Cross-sectional area [mm^2]
PRP	4.1	4.9	0.4	1.1
40% RBC	7.4	9.5	1.6	12.0

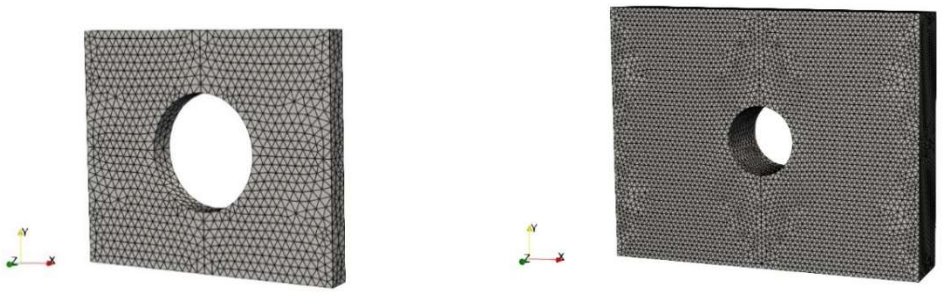

Figure 6.1: Fracture test geometries used for the PRP (left) and 40% RBC simulations (right).

6.2 Mesh

A mesh sensitivity analysis is performed for the fracture models to ensure that the results are not affected by changing the element size of the tetrahedral mesh. The same procedure as described in chapter 5 is performed for the fracture test. Different element sizes (0.1, 0.15, and 0.2 mm) are investigated to see how many elements are required to ensure reliable results. The mesh sensitivity analysis is performed on the PRP samples including an initial hole using MM181 with a PR of 0.3. The simulations are run using MPP with 4 CPUs and 32 GB RAM.

A general comparison between the different element sizes of the tetrahedral mesh for the fracture test is presented in table 6.2. A non-linear decrease of the computational time has been observed for increasing element sizes.

Table 6.2. General comparison between the different element sizes of the tetrahedral mesh for the fracture test, using the same geometry and numerical settings.

Type mesh	Element size [mm]	Number of elements	Number of nodes	Computational time [min]
Tetrahedral	0.10	55343	11706	769
	0.15	17296	4081	204
	0.20	10833	2511	111

The error between the different meshes is calculated with equation 5.1, as described in chapter 5. Different graphs displaying the nominal stress and error between the meshes at timestep 20 and 36 for both the tensile and compression tests are shown in figure 6.2. The error values are presented in table 6.3.

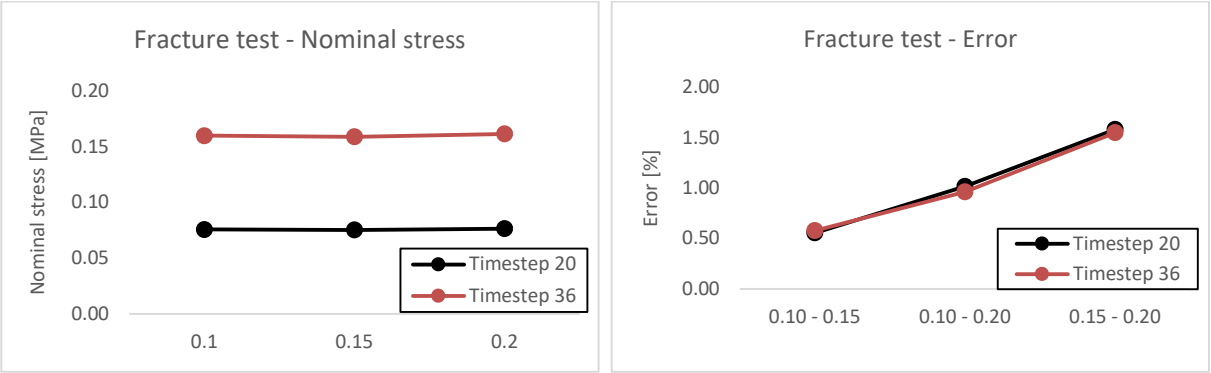

Figure 6.2: Quantitative analysis of the mesh sensitivity analysis for the fracture test. The nominal stress at timestep 20 and 36 is shown on the left for all three mesh sizes. The error in percentage between the different meshes, as calculated with equation 5.1, is shown on the right.

Table 6.3. Quantitative analysis of the mesh sensitivity analysis for the fracture test. Presented is the error between the different meshes for timestep 20 and 36.

Test	Compared meshes	Timestep	Error (%)
Fracture	0.10 – 0.15	20	0.56
		36	0.58
	0.10 – 0.20	20	1.02
		36	0.96
	0.15 – 0.20	20	1.58
		36	1.55

The maximum error for the fracture test between the 0.15 mm mesh and the finer mesh of 0.10 mm is <0.6%. This value is considered acceptable given the complexity of the geometry. Based on the error of the mesh, the computational time, and future implementation, it is chosen to continue with the tetrahedral mesh with an element size of 0.15 mm for the fracture test.

6.3 Material models

MM181 and MM295 are both used in the fracture models. The used KM values for the fracture models are found in table 6.4 and implemented in MM181. The three material parameters (C10, C20, C30) received from the fitting procedure using equation 3.3 are shown in table 6.5. These values are implemented in MM295.

Table 6.4. Linear bulk modulus (KM) values were calculated using the maximum derivative of the corresponding stress-strain curves.

Type test	Composition	KM [MPa]
Fracture	PRP	0.80
	40% RBC	0.10

Table 6.5. Material parameters that are found with the Yeoh model. These parameters are implemented in MM295 to describe the experimental curve.

Composition	C10 [MPa]	C20 [MPa]	C30 [MPa]
PRP	0.028057	0.001023	0
40% RBC	0.001012	0.000090	0.000023

6.4 Models without fracture

Fracture of the clot analogs occurs when the stress applied exceeds the threshold strength of the clot analogs. To determine this threshold strength of the clot analogs, a pre-simulation is needed to study the tensile behavior of the clots analogs without fracture. In order to do so, the stress-strain curve is extended to exclude the fracture and obtain the damage parameters (Appendix B). These parameters are necessary for the models in chapter 6.4 and 6.5. The extended stress-strain curve is used as input for MM181 and MM295.

The stress-strain curves for the numerical simulations without fracture are presented in figure 6.3 (PRP sample) and figure 6.4 (40% RBC sample). Both models underestimate the stress but behave identically for the PRP sample. A difference has been observed after a strain of 0.5 for the 40% RBC sample between MM181 and MM295.

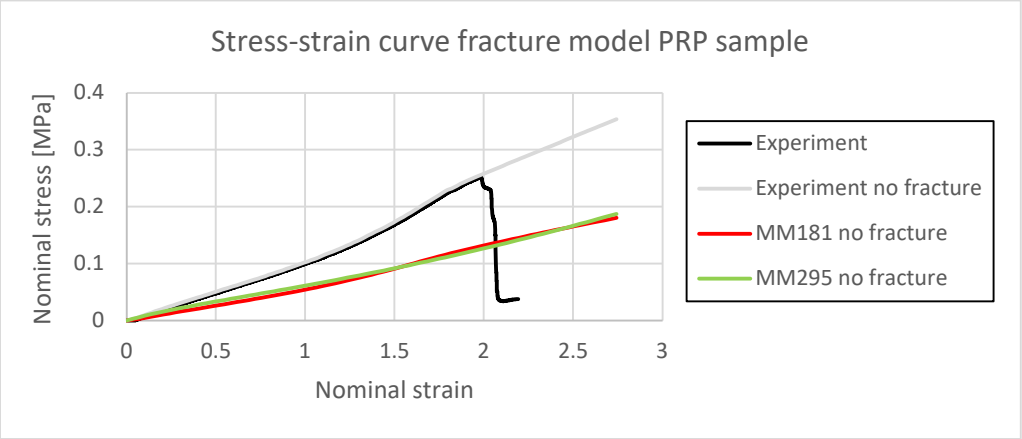

Figure 6.3: Stress-strain curve fracture model PRP sample with MM181 and MM295 without fracture.

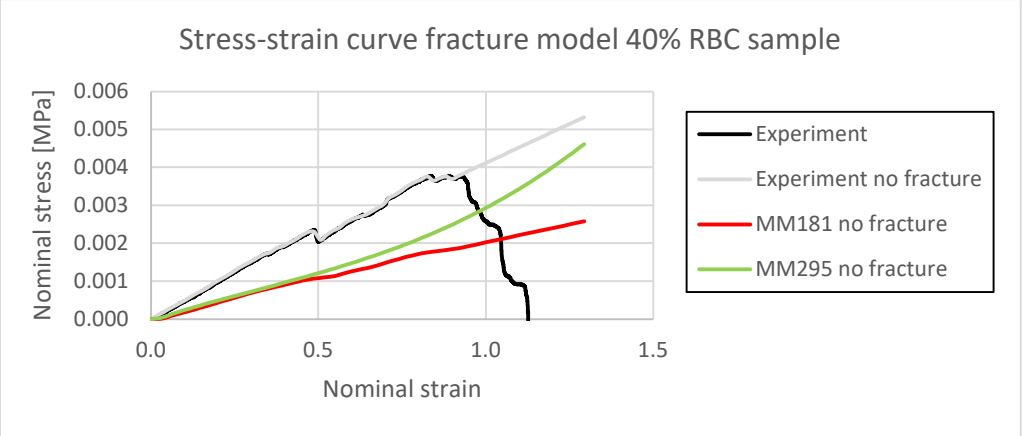

Figure 6.4: Stress-strain curve fracture model 40% RBC sample with MM181 and MM295 without fracture.

6.5 Failure model

Some material models in LS-DYNA do not have the option to include damage or failure in the material model itself. This is the case for MM295. Implementation of failure in this material model can be done by adding the keyword MAT_ADD_EROSION. This keyword can also be applied to material models that already include a damage or failure option, like MM181.

A critical failure value is used to determine the strength of the clot analog. The maximum principal stress at failure is the leading variable that defines when abrupt failure must occur.

The results from the models without fracture for both material models and clot analog compositions are used to calculate the maximum principal stress using ParaView. From the experimental stress-strain curve, the timestep where fracture occurred was derived. This corresponds with timestep 29 in the numerical models for both clot analog compositions. At this timestep, the maximum principal stress was calculated and set out in table 6.6.

The contour plot of the maximum principal stress at timestep 29 for the PRP sample using MM181 is shown in figure 6.5. The maximum principal stress is located around the hole in the central part and highlighted with the arrows. The maximum principal stress has a value of 1.06 MPa. The same procedure is performed for the 40% sample and MM295 for both clot compositions. For all models, the maximum principal stress was located around the hole. The values presented in table 6.6 are included in the keyword MAT_ADD_EROSION.

Table 6.6. Maximum principal stress values were found at timestep 29 for both material models and clot analog compositions.

Material model	Clot composition	Maximum principal stress [MPa]
MM181	PRP	1.06
	40% RBC	0.02
MM295	PRP	1.88
	40% RBC	0.04

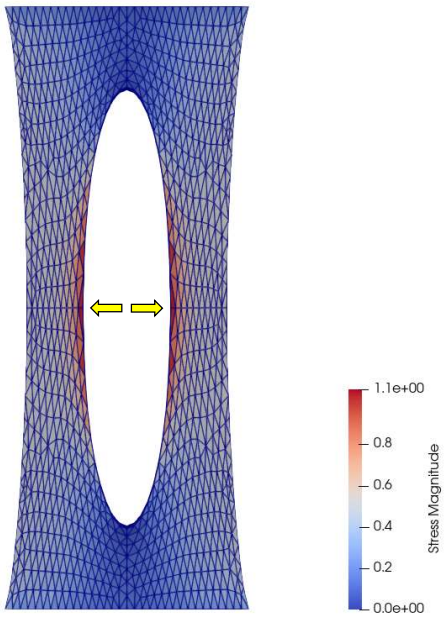

Figure 6.5: Contour plot of the maximum principal stress calculated in ParaView in the PRP sample with MM181. The maximum principal stress is achieved around the hole and has a value of 1.06 MPa.

6.5.1 Results

For both material models, numerical simulations are performed to investigate the failure option by adding the keyword MAT_ADD_EROSION in LS-DYNA.

6.5.1.1 PRP sample failure model

The stress-strain curve of the PRP sample using MM181 is shown in figure 6.6 and MM295 in figure 6.7. The no failure and with failure curves completely overlap up till the point of failure. The moment when failure should occur corresponds with the experimental data. Failure occurred where the maximum principal stress was located.

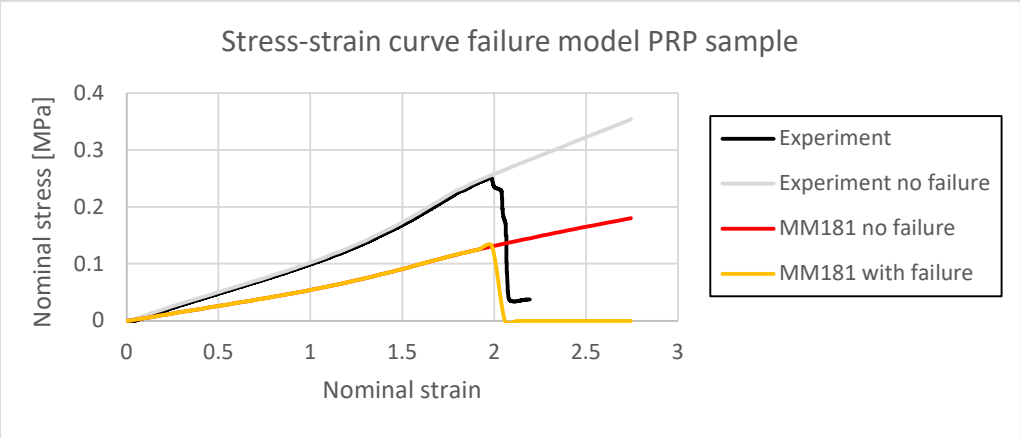

Figure 6.6: Stress-strain curve of the PRP sample and MM181, including the curve without failure and with failure by adding the keyword MAT_ADD_EROSION.

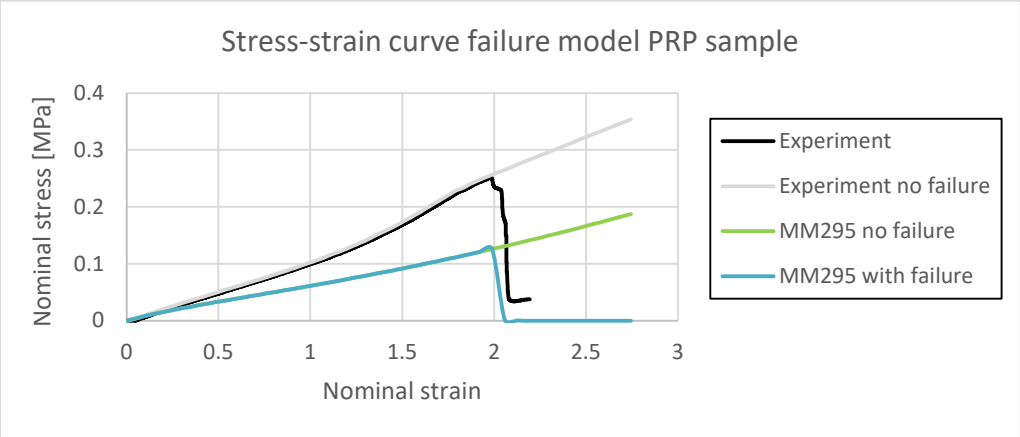

Figure 6.7: Stress-strain curve of the PRP sample and MM295, including the curve without failure and with failure by adding the keyword MAT_ADD_EROSION.

6.5.1.2 40% RBC sample failure model

The stress-strain curves for both material models including failure are shown for MM181 in figure 6.8 and for MM295 in figure 6.9. Similar to the PRP sample, no difference has been found between the no failure and failure stress-strain curves for both material models till the point of failure. The moment when failure should occur corresponds again with the experimental data. Failure occurred again where the maximum principal stress was located.

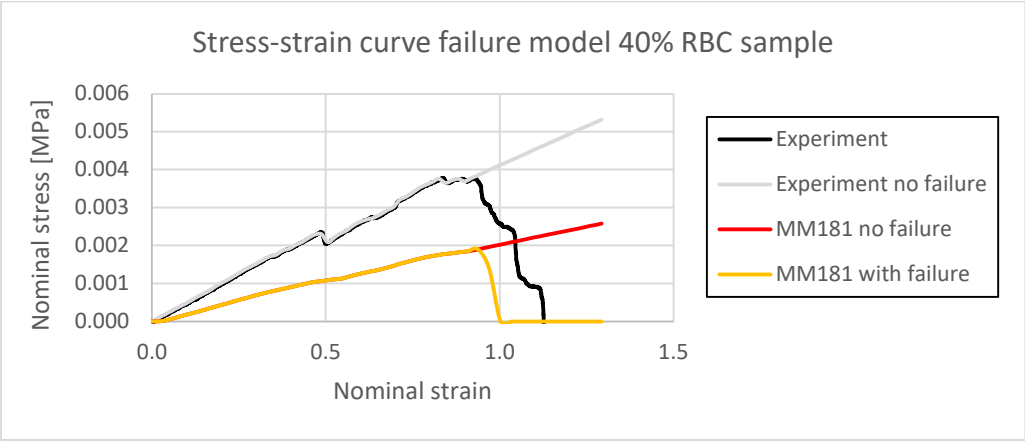

Figure 6.8: Stress-strain curve of the 40% RBC sample and MM181, including the curve without failure and with failure by adding the keyword MAT_ADD_EROSION.

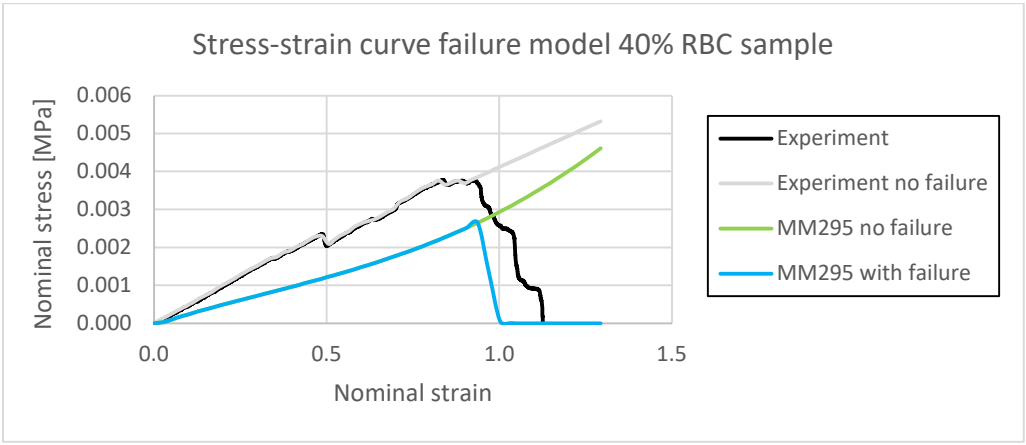

Figure 6.9: Stress-strain curve of the 40% RBC sample and MM295, including the curve without failure and with failure by adding the keyword MAT_ADD_EROSION.

6.6 Damage model

Feng and Hallquist proposed the failure criterion function for soft biological materials used in MM181 [37]. This failure criterion is useful for both small and large deformations. The general failure criterion is as follows:

$$f(I_1, I_2) = (I_1 - 3) + \Gamma_1(I_1 - 3)^2 + \Gamma_2(I_2 - 3) = K \tag{6.1}$$

with K, Γ_1 (GAMA1), and Γ_2 (GAMA2) as material failure constants.

The I_1 and I_2 are calculated with:

$$I_1 = \lambda_1^2 + \lambda_2^2 + \lambda_3^2 \tag{6.2}$$
$$I_2 = \lambda_1^2\lambda_2^2 + \lambda_2^2\lambda_3^2 + \lambda_3^2\lambda_1^2 \tag{6.3}$$

with λ_1, λ_2, and λ_3 as the three principal stretches.

The material failure constants can be determined with experimental tests followed by numerical minimization analysis. Proposed are the uniaxial tensile test, biaxial tensile test, and a variation of forces during the biaxial tensile test. Each test provides one data point on the failure surface map shown in figure 6.10. The failure strain of the uniaxial tensile test will provide a data point on the $\lambda_1\lambda_2^2 = 1$ line. The line $\lambda_1 = \lambda_2$ will provide the data point collected from the biaxial tensile test. The best-fit constants for K, GAMA1, and GAMA2 are derived with these data points and numerical minimization analysis.

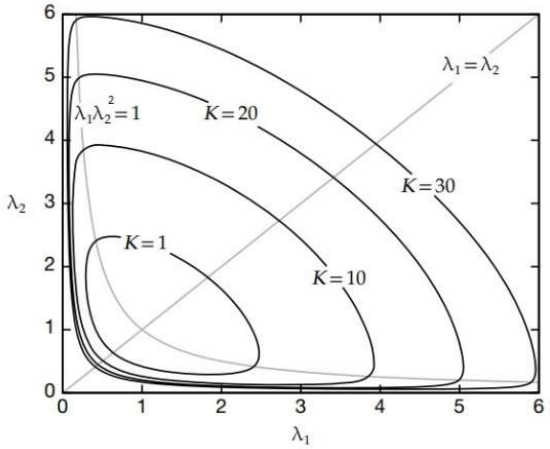

Figure 6.10: Failure surface map. More strain energy is available with a larger K value, and therefore it takes longer before the maximum strain energy is reached when material failure will occur. λ_1 is the stretch ratio in the 1-axis and λ_2 in the 2-axis [37].

The failure surface, as shown in figure 6.10, is based on the energy principle [36]. More strain energy is available with a larger K value. When the maximum strain energy is reached, material failure will occur. The K value is equivalent to the traditional strength of the material. A smaller K value results in failure that occurs faster. GAMA1 and GAMA2 specify the range where damage should take place. To accurately determine GAMA2, the biaxial test data is needed. The GAMA1 value can be determined with the uniaxial test. Unfortunately, there is no biaxial tester available in the EMC lab. Therefore, ParaView is used to determine both material failure constants.

It is hypothesized that damage occurs after reaching the ultimate strength of the clot analogs. Observed from the experimental stress-strain curves, the damage range for the 40% RBC sample is larger than the PRP sample. The 40% RBC sample with a limited number of GAMA1 and GAMA2 combinations will be used in this study to explore the possibilities of the damage model in MM181.

The LS-DYNA manual suggests to start with GAMA1 and GAMA2 set to zero to determine K [33]. Because the K value is associated with the traditional strength, the maximum K value is determined at the strain where the clot analog has its ultimate strength. This corresponds with timestep 29 in the numerical simulations. A trial and error process was set up to investigate the influence of GAMA1 and GAMA2 parameters, where a somewhat arbitrary range was used (table 6.7). The damage range for the 40% RBC sample is small, and therefore small values are used for both GAMA values to specify the range where damage should occur.

Table 6.7. Different combinations of GAMA1 and GAMA2 to investigate the maximum K value for the 40% RBC sample at timestep 29.

Version	GAMA1	GAMA2	K
V1	0.00	0.00	8.2
V2	0.01	0.00	8.9
V3	0.00	0.01	8.3
V4	0.01	0.01	9.0
V5	0.10	0.01	15.1
V6	0.01	0.10	9.7
V7	0.05	0.01	11.7
V8	0.01	0.05	9.3
V9	0.05	0.05	12.0
V10	0.20	0.01	21.8
V11	0.01	0.20	10.5
V12	0.50	0.20	43.6
V13	0.20	0.50	25.7
V14	0.20	0.20	23.3
V15	0.50	0.50	46.0

Besides K, GAMA1, and GAMA2, a fourth parameter h is used to model the process of damage growth instead of sudden failure of the material. The damage function is presented in equation 6.4. This damage function determines whether there is no damage ($D = 0$), initiation of damage ($D = \frac{1}{2}\left[1 + cos\frac{\pi(f-K)}{hK}\right]$) or fracture of the material ($D = 1$).

$$D = \begin{cases} 0 & f \leq (1-h)K \\ \frac{1}{2}\left[1 + cos\frac{\pi(f-K)}{hK}\right] & if \quad (1-h)K < f < K \\ 1 & f \geq K \end{cases} \tag{6.4}$$

The stress in the model is affected by the damage, according to the following equation:

$$\sigma_{ij} = (1-D)\sigma_{ij}^{o} \tag{6.5}$$

with σ_{ij}^{o} the undamaged stress.

There are two threshold values, $(1-h)K$ and K, where h reflects the range between damage initiation and material failure. The influence of h is shown in figure 6.11, where GAMA1 and GAMA2 were set to zero (K = 8.2). The damage range is the largest when using an h value of 0.5, but the time from damage initiation till material failure is still very fast. Thereby, a large h value results in earlier damage initiation and consequently in earlier onset of fracture compared to the experimental data. Because the damage range is so small for all h values, it is chosen to continue with an h value of 0.01. This value has the best agreement with the onset of damage compared to the experimental data.

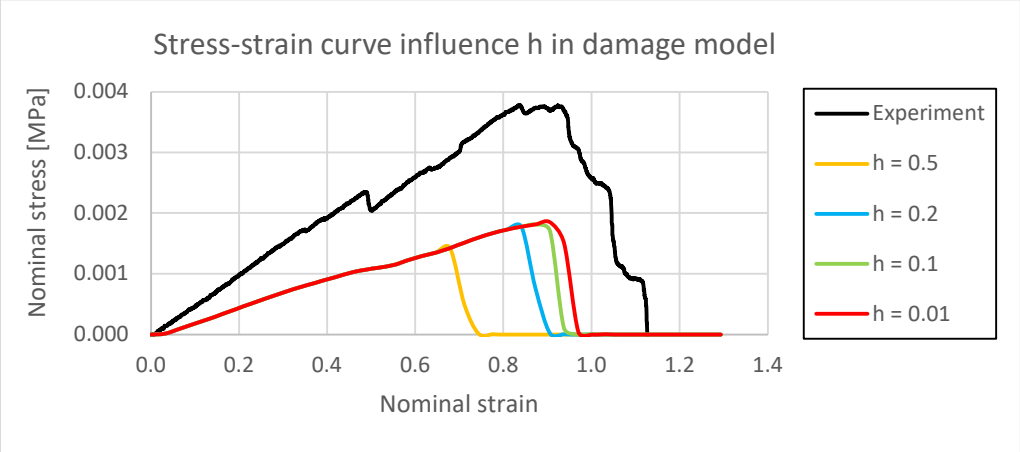

Figure 6.11: The influence of a different h value, which represents the process of damage growth in the damage function. A larger h value results in earlier onset of the damage and eventually fracture.

6.6.1 Results

A total of fifteen different simulations are performed to investigate the effect of increasing the value of GAMA1 and GAMA2 on the damage evolution in the 40% RBC model. First the effect of when GAMA1 and GAMA2 are equal. Version 1, 9, 14, and 15 are compared to each other. The differences between the different versions are hard to see in figure 6.12. Therefore in figure 6.13, a zoomed-in version of the stress-strain curve is presented. The K value in version 1 is the smallest of all versions, and this model has the earliest onset of damage compared to the other versions. Further increasing the GAMA values (and corresponding K values), but keeping them equal, results in later onset of damage. A slight increase in the nominal stress is visible in all versions before damage occurs (figure 6.13).

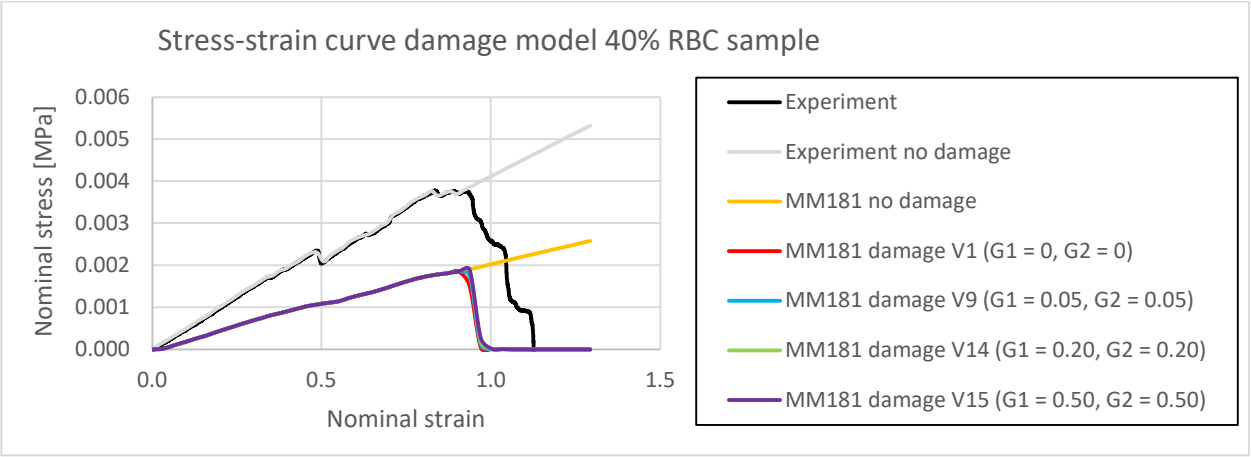

Figure 6.12: Stress-strain curves of the versions where GAMA1 and GAMA2 are equal, respectively version 1, 9, 14, and 15.

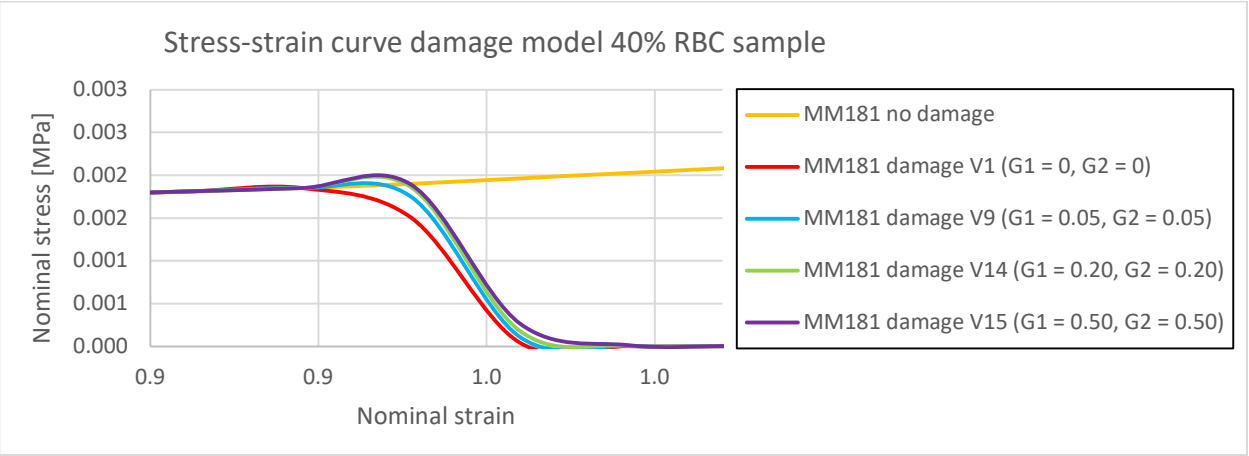

Figure 6.13: Zoomed in version of figure 6.12 to show the differences between versions 1, 9, 14, and 15.

To investigate which GAMA value influences the outcome, five versions where the GAMA values differed are investigated next. Versions 4, 7, 8, 10, and 11 are shown in figure 6.14. A zoomed-in version of figure 6.14 is shown in figure 6.15 to make the differences more visible. The difference in percentage at three different strain levels (0.9, 0.95, and 1.0) between version 7, 8, 10, and 11 compared to version 4 is presented in table 6.8. Increasing GAMA1 (version 7 and 10) results in a later onset of the damage compared to version 4. The difference at a strain of 0.9 is 0% for both versions, but a difference of 9.1% and 54.7% for version 7 and 14.8% and 77.4% for version 11 are found at respectively a strain of 0.95 and 1.0. Increasing GAMA2 (version 8 and 11) does not result in any difference at a strain of 0.9, but a small difference of 0.7% and 0.8% for version 8 and 1.8% and 0.2% for version 11 are found at respectively a strain of 0.95 and 1.0.

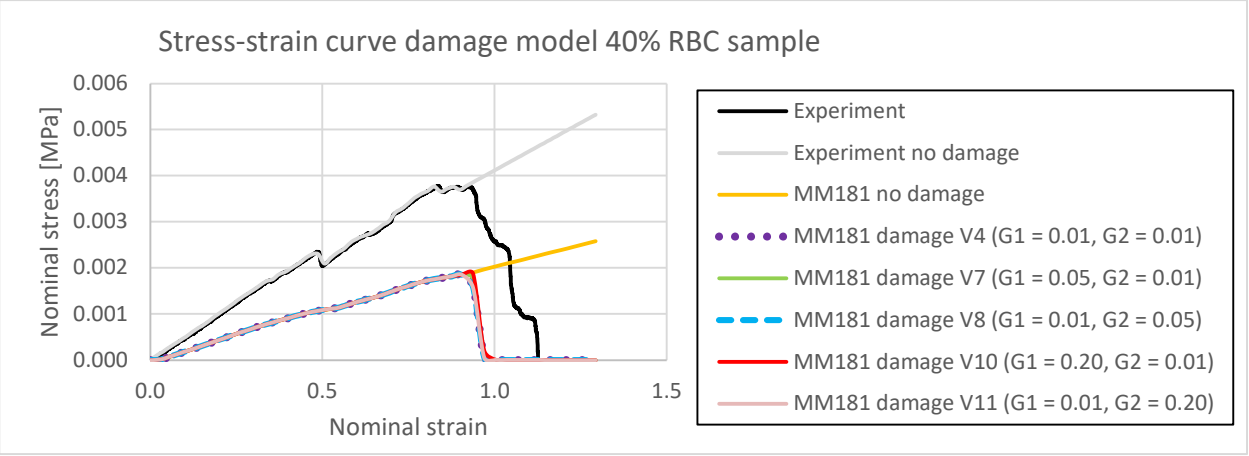

Figure 6.14: Stress-strain curves when the GAMA values are not equal (version 7, 8, 10, and 11) and when they are equal (version 4).

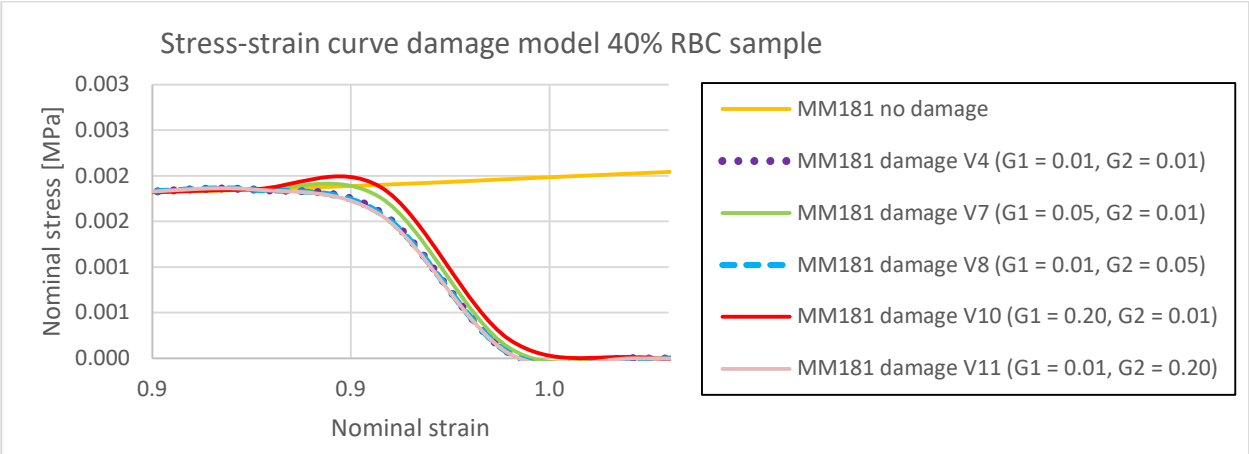

Figure 6.15: Zoomed in version of the stress-strain curves when the GAMA values are not equal (version 7, 8, 10, and 11) and when they are equal (version 4).

Table 6.8. At three strain values (0.9, 0.95, and 1.0), the difference in percentage between version 7, 8, 10, and 11 compared to version 4 is calculated.

Strain	Version 7	Version 8	Version 10	Version 11
0.9	0.0%	0.0%	0.0%	0.0%
0.95	9.1%	0.7%	14.8%	1.8%
1.0	54.7%	0.8%	77.4%	0.2%

6.7 Discussion

The last chapter of this study focused on the fracture mechanics of the thrombus. Two different options to add fracture to the model were investigated: the failure and damage model.

Including failure to the thrombus model was successfully performed by adding the keyword MAT_ADD_EROSION. The maximum principal stress was used as a critical value and located around the hole in the central part. As expected, fracture of the clot analog occurred at the same location.

The damage model in MM181 was used to include damage prior to failure of the clot analog. Four material failure constants determine the range between damage initiation and material failure. The results from the damage model in this study can be summarized in four main findings. First, a larger K value results in later onset of failure. Second, increasing GAMA1 results in a later onset of damage, but the range between damage initiation and fracture decreases. Third, the influence of GAMA2 on the damage initiation is negligibly small. Last, the range between damage initiation and material failure is larger with a larger h value and results in an earlier onset of damage and fracture compared to the experimental data.

A limited number of GAMA1 and GAMA2 combinations are used in this study to explore the possibilities of the damage model in MM181. Increasing the value of GAMA1 results in a negligibly small damage range. The influence of GAMA2 on the range of damage initiation and fracture was almost imperceptible in the 40% RBC sample. The theoretical influence of GAMA2 on the material failure surface is illustrated in figure 6.17 [37]. Increasing GAMA2 should decrease the failure surface and, as a result, earlier onset of failure. That this is not observable in the numerical models probably has to do with the experimental data.

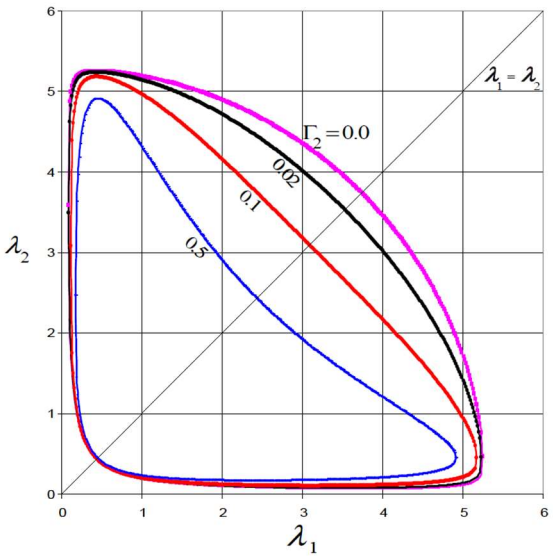

Figure 6.17: Impact of GAMA2 on the material failure surface. Increasing GAMA2 results in a smaller failure surface map and earlier onset of failure [37].

In conclusion, MM181 can model the range between damage initiation and material failure, but the experimental data used in this study did not allow us to observe the true impact of K, GAMA1, GAMA2, and h on the damage model. The findings from the results in this study depend on the experimental data available and how the parameters were obtained. The experimental stress-strain curve of the 40% RBC sample already showed that the range between damage initiation and material failure was not very large. Therefore, the impact of the various material failure constants is more challenging to determine.

7 Discussion

This study was performed to develop a computational thrombus model using finite element software LS-DYNA. The mechanical behavior of the clot analogs under tensile and compressive loading conditions was examined. Three models (cube model, geometry model, and fracture model) were developed to gain insight into the possibilities within LS-DYNA.

Cube model

The cube models were developed to select material models capable of describing the mechanical behavior of the clot analogs. Two different material models were explored, MM181 with the option to include damage and MM295 with the option to include anisotropy. Because the PR value for a solid thrombus model was not defined yet in the literature, different PRs were used to investigate which one was the best option to describe the mechanical behavior of the thrombus. The results of the cube models can be summarized in three main findings. First, MM181 with a PR of 0.30 and MM295 with a PR of 0.49 were capable of describing the non-linear behavior under compressive and tensile loading conditions at both low and high strains. Second, both material models were capable of describing the behavior of the clot analogs with different compositions, although it should be noted that the stresses in the 40% RBC sample were much lower than in the PRP sample. Third, MM181 with a PR of 0.30 was capable of combining both tensile and compressive loading conditions in one model. From these findings, it can be concluded that considering the settings used, the cube models in this study can describe the mechanical behavior of thrombi with different clot compositions under tensile and compressive loading conditions.

The first finding of this study is in line with previous literature, the capability of MM181 with a PR of 0.30 to describe the mechanical behavior of the clot analog under compressive and tensile loading conditions. Luraghi *et al.* developed a numerical thrombus model using MM181 and a PR of 0.30 in LS-DYNA [22]. They developed a model that simulates the mechanical thrombectomy procedure, in which the clot analog was subjected to both compressive and tensile loading. The researchers were capable of reproducing the experimental results accurately. It, therefore, seems that this material model is suitable for describing compressive and tensile behavior.

Regarding the second finding, it was observed in this study that the numerical models predicted very low stresses for the 40% RBC samples under compression. The experimental data also revealed this, and because of the noise, there were occasional negative values for the 40% RBC clot analogs up to a strain of 50%. Distinguishing between the signal and the measurement equipment's noise signal is very difficult at such low stresses. Therefore the negative values were replaced by zero values, and as a result, the stress-strain curve slightly changed. This might have an impact on the fitting procedure for both MM181 and MM295 because a more artificial looking curve has been used. The empirical curve fitting procedure differs for both material models. Very little information was available about the fitting procedure in MM181. The LS-DYNA volume manual did not provide any information about how the fitting procedure was performed in MM181. Additional information came from the paper of Luraghi *et al.,* where they described that MM181 uses a function to fit the uniaxial stress-strain curve internally [22]. The quality of the fit with the experimental data in this internal fitting procedure is unknown. It is therefore strongly advised to investigate this in future studies. Empirical curve fitting to obtain the material parameters for MM295 is performed using a MATLAB script that assumes that the material is incompressible. Given this fact, it is therefore not surprising that a PR of 0.49 shows the best fit in MM295 for both the compression and tensile test. The PR could be changed, but therefore the entire script must be rewritten. Future studies should consider this fact and possibly rewrite the script to use it for compressible materials like a thrombus.

As stated in the third finding, the cube combination model that has been run using MM181 with a PR of 0.3 for the PRP sample with an asymmetric stress-strain curve as input showed promising results. Regardless of the order of the loading conditions, the numerical models could describe both the tensile and compressive behavior. Combining compression and tension in one model was not possible with MM295. The reason is unclear and needs further investigation. The fact that the model works so well with MM181 is therefore beneficial for future implementations.

Geometry model

The geometry models were developed to mimic the geometry of the experimental samples used in the tensile and compression test, where an idealized geometry was used. In accordance with previous literature, these geometries were meshed with tetrahedral elements [17-18][22]. The results of the geometry models can be summarized in two main findings. First, MM181 and MM295 can describe the clot analog behavior under tensile loading conditions, but the choice of the simplified geometry resulted in lower nominal stress values than the experimental data. Second, both material models have problems describing the mechanical behavior of the clot analog under compressive loading conditions.

Lower nominal stress was obtained during the tensile test for the numerical models compared to the experimental test data. Recalling the good comparison between the experimental data and the two numerical models in the cube model, this discrepancy in the geometry model could be linked to the geometry. The geometry used in the numerical models is different compared to the geometry of the experimental samples. This difference in geometry will affect the resultant force and thus the stress in the numerical models. The numerical models predict the shape of the experimental stress-strain curve very well, but in general, the stresses are severely underestimated. This can potentially be solved by using the same geometry in the numerical models and experiments.

From the mesh sensitivity analysis, it could be concluded that it is necessary to be careful when interpreting the compression test results at high strains. After a strain of 0.6, the quality of the tetrahedral elements was not preserved. The large differences between the numerical models and experimental data at high strains were therefore not unexpected. Nevertheless, there is also a discrepancy at the low strain regions between both material models and the experimental data, where MM181 underestimates the stress and MM295 overestimates the stress. The mesh quality with an element size of 0.3 mm was relatively good in these low strain regions, so there must be a different reason for the observed differences. The reason is unclear and needs further investigation.

Fracture model

The fracture models in this study can contribute to a better understanding of thrombus fragmentation. The results of the fracture models can be summarized in two main findings. First, fracture of the clot analogs was successfully achieved by implementing the maximum principal stress as a critical value. Second, the inclusion of the damage model resulted in fracture of the clot analog, but the intended damage evolution in the clot analog was not observed.

The damage range of the experimental data of both the PRP and 40% RBC sample was minimal and material failure followed soon. Because the damage range was minimal, the impact of the damage parameters (GAMA1 and GAMA2) was hard to observe. The stress in the implemented damage model should decrease from a certain value compared to the calculation without damage. Contrary to what the damage model implies, almost abrupt fracture has been observed in this study. This could have been caused by how the material parameters were obtained. In this study, the parameter estimation was based on ParaView, while it is advised to use experimental data [37]. Unfortunately, these experimental data were not available.

It was hypothesized that damage occurred after reaching the ultimate strength of the clot analogs, but the exact timestep cannot be determined from the experimental data. It could be possible that damage occurs earlier, with changes in the fibrous network under tension. This is in agreement with previous literature, which found that under tensile loading, the fibrin fibers started to stretch more than four times their unloaded length before fracture [38]. In addition, in silico studies found fiber alignment beyond and at the crack tip [25-26]. More detailed experiments are needed to determine the onset of damage and implement damage with the damage model in MM181 instead of only modeling failure.

Future work

This study provides a framework for modeling a thrombus under tensile and compressive loading, where the thrombus was modeled as a hyperelastic material. This framework allows for further improvements.

First, it is advised to include the property of viscoelasticity. The viscoelasticity determines the ability of the thrombus to deform. This is important, for example, when using a stent-retriever during mechanical thrombectomy, where the thrombus must be integrated within the stent struts. In vivo thrombi are viscoelastic materials, and by defining the material properties of the thrombus as viscoelastic rather than hyperelastic, a more realistic numerical model can be developed. The first steps to model the thrombus as a viscoelastic material have been taken by a recent in silico study. Johnson *et al.* investigated the stress relaxation and loading-unloading hysteresis [24]. These two viscoelastic characteristics required two different experiments. A constant compressive load was applied to determine the stress relaxation. Application of 10 cycles of 80% compression at a constant strain rate was used to determine the loading-unloading hysteresis. The researchers found a good comparison between the experimental data and the numerical models, where the thrombus was modeled as a viscoelastic material.
Including viscoelasticity is impossible in MM295 because this material model is only suitable for hyperelastic materials. However, implementing the viscoelasticity is possible with MM181. The compression test experiments in this study were performed with 80% compression for 20 cycles at a constant strain rate. Using this data to investigate the loading-unloading hysteresis with MM181 in LS-DYNA is interesting.

Second, the thrombus models developed in this study are only exposed to tensile and compressive forces. During mechanical thrombectomy, the thrombus will also be exposed to friction and shear forces [12]. The friction forces are affected by the thrombus composition, where a higher clot friction coefficient has been found for the fibrin rich clot analogs compared to the RBC rich clot analogs [39]. No in silico thrombus model has been developed yet that investigates the influence of friction between the thrombus and the vessel wall. Sugerman *et al.* investigated the mechanical behavior of the thrombus under shear stress in a numerical thrombus model [40]. The thrombus was modeled with a regular shape, homogeneous, and as a hyperelastic material. The researchers were capable of describing shear stress under large deformations.
The approach used by Sugerman *et al.* is the same as used in this thesis. The results of the study of Sugerman *et al.* offer possibilities for applying shear stress within the models in LS-DYNA.

Third, a thrombus in vivo is heterogeneous, and this heterogeneity influences the thrombus (fracture) mechanics, as already stated in chapter 2.6. In the future, an attempt must be made to include heterogeneity in the models in order to fully understand the influence of composition on the thrombus mechanics. In silico mechanical thrombectomy models will benefit from this change in composition of the thrombus, especially when patient specific in silico models will be developed. A regular shape is used as geometry for the in silico thrombus models, but in reality, the thrombus has an irregular complex shape. This shape could cause higher local stresses in some regions of the thrombus that may fracture earlier than other parts [25].

Last, this solid thrombus model can be extended by implementing additional parts, i.e., an aspiration catheter, balloon guided catheter, or a stent-retriever [41]. These devices are used during mechanical thrombectomy in order to remove the thrombus. In addition, with LS-DYNA it is possible to add the fluid domain. Better understanding the fluid-structure interaction between the thrombus, blood, balloon guided catheter, aspiration catheter, stent-retriever, and vessel wall is of great value.

8 Conclusion

This study provides a framework for modeling the thrombus under tensile and compressive loading, where the thrombus is modeled as a hyperelastic material. To investigate the mechanical behavior under both compressive and tensile loading conditions, numerical models were developed using LS-DYNA. Two material models successfully described the thrombus's non-linear behavior in both the cube and geometry models. MM181 with a PR of 0.30 and MM295 with a PR of 0.49 resulted in the best agreement between the experimental data and numerical models. The combination of both tension and compression in the cube model was successfully implemented by using MM181 with a PR of 0.30. The Yeoh model in MM295 could not model both loading conditions in one model. Both the damage and failure models could describe the thrombus fracture mechanics. It was expected that the stress would gradually decrease for the damage model, but abrupt fracture was observed. This behavior was similar to the failure model that used a critical value that determined when failure must occur. The numerical thrombus models developed in this study have delivered useful information about the two material models and the basic components of LS-DYNA. It allows for further improvements that could ultimately lead to the development of patient specific in silico models.

References

[1] Virani, S. S., Alonso, A., Benjamin, E. J., Bittencourt, M. S., Callaway, C. W., Carson, A. P., … Tsao, C. W. (2020). Heart Disease and Stroke Statistics—2020 Update: A Report From the American Heart Association. *Circulation*, *141*(9), 216–261. https://doi.org/10.1161/cir.0000000000000757

[2] Nordin, K. M., Chellappan, K., & Sahathevan, R. (2014). Upper limb rehabilitation in post stroke patients: Clinical observation. *2014 IEEE Conference on Biomedical Engineering and Sciences (IECBES)*. https://doi.org/10.1109/iecbes.2014.7047597

[3] Staessens, S., Denorme, F., Francois, O., Desender, L., Dewaele, T., Vanacker, P., … De Meyer, S. F. (2019). Structural analysis of ischemic stroke thrombi: histological indications for therapy resistance. *Haematologica*, *105*(2), 498–507. https://doi.org/10.3324/haematol.2019.219881

[4] Yazdani, A., Li, H., Humphrey, J. D., & Karniadakis, G. E. (2017). A General Shear Dependent Model for Thrombus Formation. *PLOS Computational Biology*, *13*(1), e1005291. https://doi.org/10.1371/journal.pcbi.1005291

[5] Boodt, N., Snouckaert Van Schauburg, P. R., Hund, H. M., Fereidoonnezhad, B., McGarry, J. P., Akyildiz, A. C., van Es, A. C., de Meyer, S. F., Dippel, D. W., Lingsma, H. F., van Beusekom, H. M., van der Lugt, A., & Gijsen, F. J. (2021). Mechanical Characterization of Thrombi Retrieved With Endovascular Thrombectomy in Patients With Acute Ischemic Stroke. *Stroke*, *52*(8), 2510–2517. https://doi.org/10.1161/strokeaha.120.033527

[6] Marder, V. J., Chute, D. J., Starkman, S., Abolian, A. M., Kidwell, C., Liebeskind, D., … Saver, J. L. (2006). Analysis of Thrombi Retrieved From Cerebral Arteries of Patients With Acute Ischemic Stroke. *Stroke*, *37*(8), 2086–2093. https://doi.org/10.1161/01.str.0000230307.03438.94

[7] Johnson, S., Duffy, S., Gunning, G., Gilvarry, M., McGarry, J. P., & McHugh, P. E. (2017). Review of Mechanical Testing and Modelling of Thrombus Material for Vascular Implant and Device Design. *Annals of Biomedical Engineering*, *45*(11), 2494–2508. https://doi.org/10.1007/s10439-017-1906-5

[8] Krasokha, N., Theisen, W., Reese, S., Mordasini, P., Brekenfeld, C., Gralla, J., … Monstadt, H. (2010). Mechanical properties of blood clots - a new test method. *Materialwissenschaft Und Werkstofftechnik*, *41*(12), 1019–1024. https://doi.org/10.1002/mawe.201000703

[9] Lambrinos, A., Schaink, A. K., Dhalla, I., Krings, T., Casaubon, L. K., Sikich, N., … Hill, M. D. (2016). Mechanical Thrombectomy in Acute Ischemic Stroke: A Systematic Review. *Canadian Journal of Neurological Sciences / Journal Canadien Des Sciences Neurologiques*, *43*(4), 455–460. https://doi.org/10.1017/cjn.2016.30

[10] Berkhemer, O. A., Fransen, P. S. S., Beumer, D., van den Berg, L. A., Lingsma, H. F., Yoo, A. J., … Dippel, D. W. J. (2015). A Randomized Trial of Intraarterial Treatment for Acute Ischemic Stroke. *New England Journal of Medicine*, *372*(1), 11–20. https://doi.org/10.1056/nejmoa1411587

[11] Kühn, A. L., Vardar, Z., Kraitem, A., King, R. M., Anagnostakou, V., Puri, A. S., & Gounis, M. J. (2020). Biomechanics and hemodynamics of stent-retrievers. *Journal of Cerebral Blood Flow & Metabolism*, 0271678X2091600. https://doi.org/10.1177/0271678x20916002

[12] Liu, Y., Zheng, Y., Reddy, A. S., Gebrezgiabhier, D., Davis, E., Cockrum, J., … Savastano, L. E. (2020). Analysis of human emboli and thrombectomy forces in large-vessel occlusion stroke. *Journal of Neurosurgery*, 1–9. https://doi.org/10.3171/2019.12.jns192187

[13] Duffy, S., Farrell, M., McArdle, K., Thornton, J., Vale, D., Rainsford, E., Morris, L., Liebeskind, D. S., MacCarthy, E., & Gilvarry, M. (2016). Novel methodology to replicate clot analogs with diverse composition in acute ischemic stroke. *Journal of NeuroInterventional Surgery*, *9*(5), 486–491. https://doi.org/10.1136/neurintsurg-2016-012308

[14] Cahalane, R., Boodt, N., Akyildiz, A. C., Giezen, J. A., Mondeel, M., van der Lugt, A., Marquering, H., & Gijsen, F. (2021). A review on the association of thrombus composition with mechanical and radiological imaging characteristics in acute ischemic stroke. *Journal of Biomechanics*, *129*, 110816. https://doi.org/10.1016/j.jbiomech.2021.110816

[15] Machi, P., Jourdan, F., Ambard, D., Reynaud, C., Lobotesis, K., Sanchez, M., … Costalat, V. (2016). Experimental evaluation of stent retrievers' mechanical properties and effectiveness. *Journal of NeuroInterventional Surgery*, *9*(3), 257–263. https://doi.org/10.1136/neurintsurg-2015-012213

[16] Konduri, P. R., Marquering, H. A., van Bavel, E. E., Hoekstra, A., & Majoie, C. B. L. M. (2020). In-Silico Trials for Treatment of Acute Ischemic Stroke. *Frontiers in Neurology*, *11*. https://doi.org/10.3389/fneur.2020.558125

[17] Luraghi, G., Cahalane, R. M., van de Ven, E., Overschie, S. C. M., Gijsen, F. J., & Akyildiz, A. C. (2021). In vitro and in silico modeling of endovascular stroke treatments for acute ischemic stroke. *Journal of Biomechanics*, *127*, 110693. https://doi.org/10.1016/j.jbiomech.2021.110693

[18] Talayero, C., Romero, G., Pearce, G., & Wong, J. (2019). Numerical modelling of blood clot extraction by aspiration thrombectomy. Evaluation of aspiration catheter geometry. *Journal of Biomechanics*, *94*, 193–201. https://doi.org/10.1016/j.jbiomech.2019.07.033

[19] Romero, G., Martinez, M. L., Maroto, J., & Pearce, G. (2012). A Comparison of the Removal of Blood Clots by Mechanical Thrombectomy Devices using Auto-Expandable Stents and Suction Pressure Devices. *International Journal of Simulation Systems Science & Technology*, 1. https://doi.org/10.5013/ijssst.a.13.02.09

[20] Good, B. C., Simon, S., Manning, K., & Costanzo, F. (2019). Development of a computational model for acute ischemic stroke recanalization through cyclic aspiration. *Biomechanics and Modeling in Mechanobiology*, *19*(2), 761–778. https://doi.org/10.1007/s10237-019-01247-w

[21] Gu, X., Qi, Y., Erdman, A., & Li, Z. (2017). The Role of Simulation in the Design of a Semi-Enclosed Tubular Embolus Retrieval. *Journal of Medical Devices*, *11*(2). https://doi.org/10.1115/1.4036286

[22] Luraghi, G., Rodriguez Matas, J. F., Dubini, G., Berti, F., Bridio, S., Duffy, S., Dwivedi, A., McCarthy, R., Fereidoonnezhad, B., McGarry, P., Majoie, C. B. L. M., & Migliavacca, F. (2020). Applicability assessment of a stent-retriever thrombectomy finite-element model. *Interface Focus*, *11*(1), 20190123. https://doi.org/10.1098/rsfs.2019.0123

[23] Luraghi, G., Bridio, S., Rodriguez Matas, J. F., Dubini, G., Boodt, N., Gijsen, F. J., van der Lugt, A., Fereidoonnezhad, B., Moerman, K. M., McGarry, P., Konduri, P. R., Arrarte Terreros, N., Marquering, H. A., Majoie, C. B., & Migliavacca, F. (2021b). The first virtual patient-specific thrombectomy procedure. *Journal of Biomechanics*, *126*, 110622. https://doi.org/10.1016/j.jbiomech.2021.110622

[24] Johnson, S., McCarthy, R., Gilvarry, M., McHugh, P. E., & McGarry, J. P. (2020). Investigating the Mechanical Behavior of Clot Analogues Through Experimental and Computational Analysis. *Annals of Biomedical Engineering*, *49*(1), 420–431. https://doi.org/10.1007/s10439-020-02570-5

[25] Tutwiler, V., Singh, J., Litvinov, R. I., Bassani, J. L., Purohit, P. K., & Weisel, J. W. (2020). Rupture of blood clots: Mechanics and pathophysiology. *Science Advances*, *6*(35), eabc0496. https://doi.org/10.1126/sciadv.abc0496

[26] Fereidoonnezhad, B., Dwivedi, A., Johnson, S., McCarthy, R., & McGarry, P. (2021). Blood clot fracture properties are dependent on red blood cell and fibrin content. *Acta Biomaterialia*, *127*, 213–228. https://doi.org/10.1016/j.actbio.2021.03.052

[27] Abaqus (Student edition) [Computer software] (2019).

[28] Ansys Fluent (R1) [Computer software] (2021).

[29] LS-DYNA (V4.8.11) [Computer software] (2021).

[30] Giezen, J. (2021). The association between in vitro human thrombi composition, mechanics, and computed tomography imaging characteristics. [Masterscriptie, TU Delft]. Repository TU Delft. http://resolver.tudelft.nl/uuid:b317798f-a1e3-4675-890f-0049bf6dbd85

[31] Johnson, S., Chueh, J., Gounis, M. J., McCarthy, R., McGarry, J. P., McHugh, P. E., & Gilvarry, M. (2019). Mechanical behavior of in vitro blood clots and the implications for acute ischemic stroke treatment. *Journal of NeuroInterventional Surgery*, *12*(9), 853–857. https://doi.org/10.1136/neurintsurg-2019-015489

[32] Pei, M., Zou, D., Gao, Y., Zhang, J., Huang, P., Wang, J., Huang, J., Li, Z., & Chen, Y. (2021). The influence of sample geometry and size on porcine aortic material properties from uniaxial tensile tests using custom-designed tissue cutters, clamps and molds. *PLOS ONE*, *16*(2), e0244390. https://doi.org/10.1371/journal.pone.0244390

[33] Livermore Software Technology Corporation (LSTC), Keyword User's Manual Volume 2 Material Models. 2021, R.12, p. 1131.

[34] Vitello, D. J., Ripper, R. M., Fettiplace, M. R., Weinberg, G. L., & Vitello, J. M. (2015). Blood Density Is Nearly Equal to Water Density: A Validation Study of the Gravimetric Method of Measuring Intraoperative Blood Loss. *Journal of Veterinary Medicine*, *2015*, 1–4. https://doi.org/10.1155/2015/152730

[35] Yeoh, O. H. (1990). Characterization of Elastic Properties of Carbon-Black-Filled Rubber Vulcanizates. *Rubber Chemistry and Technology*, *63*(5), 792–805. https://doi.org/10.5254/1.3538289

[36] Yang, K. H. (2018). Isoparametric Formulation and Mesh Quality. *Basic Finite Element Method as Applied to Injury Biomechanics*, 111–149. https://doi.org/10.1016/b978-0-12-809831-8.00003-9

[37] Feng, W.W., Hallquist, J.O. (2005). A Failure Criterion for Polymers and Soft Biological Materials, In: 5th European LS-DYNA Users Conference Birmingham Material Technology, Birmingham, UK, 25–26 May 2005, 2b–15.

[38] Kim, O. V., Litvinov, R. I., Weisel, J. W., & Alber, M. S. (2014). Structural basis for the nonlinear mechanics of fibrin networks under compression. *Biomaterials*, *35*(25), 6739–6749. https://doi.org/10.1016/j.biomaterials.2014.04.056

[39] Gunning, G. M., McArdle, K., Mirza, M., Duffy, S., Gilvarry, M., & Brouwer, P. A. (2017). Clot friction variation with fibrin content; implications for resistance to thrombectomy. *Journal of NeuroInterventional Surgery*, *10*(1), 34–38. https://doi.org/10.1136/neurintsurg-2016-012721

[40] Sugerman, G. P., Kakaletsis, S., Thakkar, P., Chokshi, A., Parekh, S. H., & Rausch, M. K. (2021). A whole blood thrombus mimic: Constitutive behavior under simple shear. *Journal of the Mechanical Behavior of Biomedical Materials*, *115*, 104216. https://doi.org/10.1016/j.jmbbm.2020.104216

[41] Kühn, A. L., Vardar, Z., Kraitem, A., King, R. M., Anagnostakou, V., Puri, A. S., & Gounis, M. J. (2020). Biomechanics and hemodynamics of stent-retrievers. *Journal of Cerebral Blood Flow & Metabolism*, 0271678X2091600. https://doi.org/10.1177/0271678x20916002

Appendix A: Experimental data

Multiple experiments were performed to collect data sets. Not all experiments resulted in valuable results. In this appendix, six figures are included, one for each composition and test. The tensile test curves are presented in figure A.1 (PRP sample) and figure A.2 (40% RBC sample). The fracture test curves are presented in figure A.3 (PRP sample) and figure A.4 (40% RBC sample). The compression test curves are presented in figure A.5 (PRP sample) and figure A.6 (40% RBC sample).
The selected curves for each model are displayed in table A.1. A curve in the middle has been chosen to select a representative curve of the variation we have seen.

Table A.1. Selected data from all the data sets.

Test	PRP	40% RBC
Tensile	4-6-2021	4-6-2021
Fracture	22-4-2021	22-4-2021
Compression	8-4-2021 S2	17-3-2021

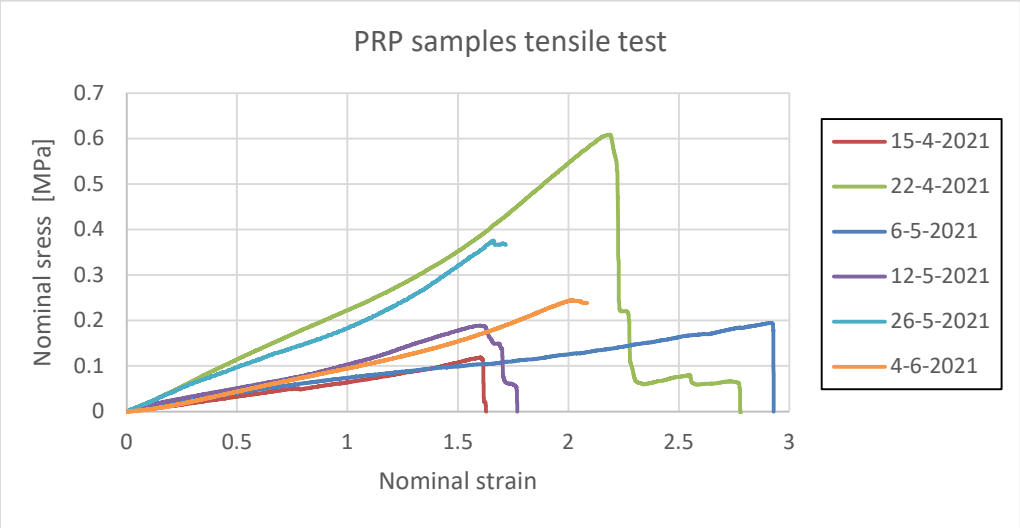

Figure A.1: Stress-strain curves from all the tensile test experiments performed with the PRP samples.

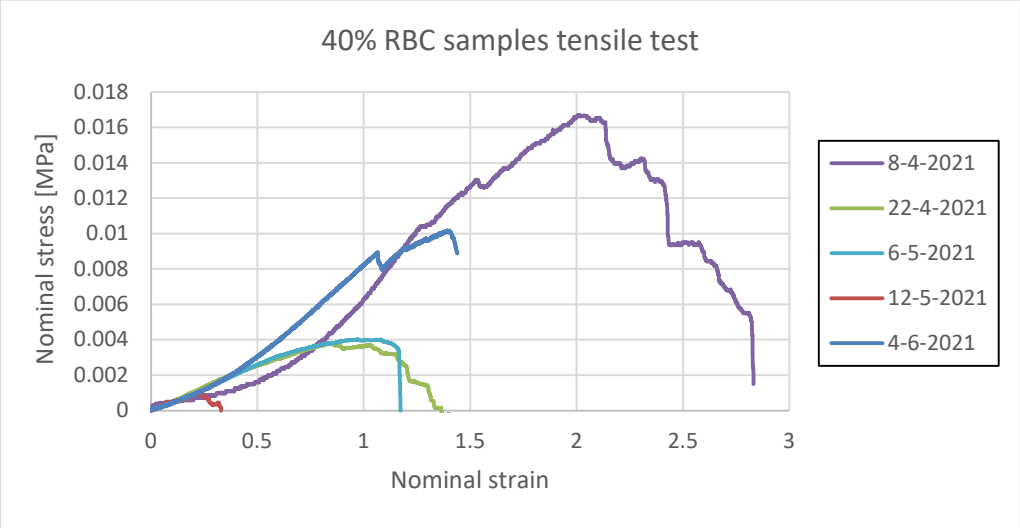

Figure A.2: Stress-strain curves from all the tensile test experiments performed with the 40% RBC samples.

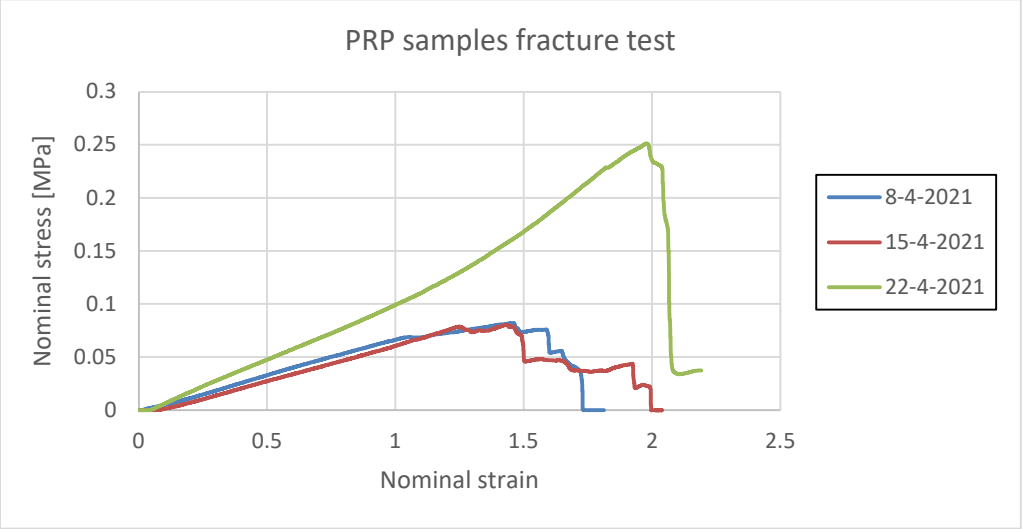

Figure A.3: Stress-strain curves from all the fracture test experiments performed with the PRP samples.

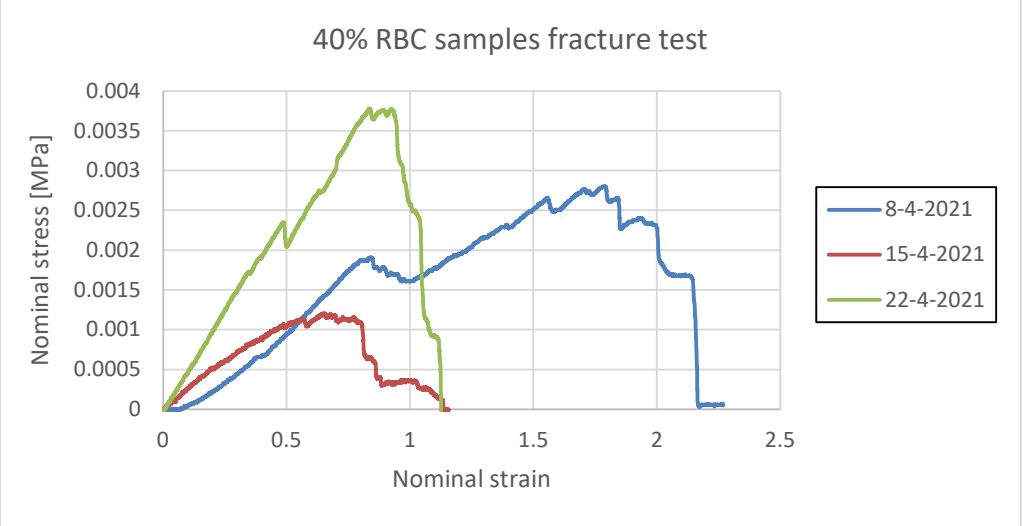

Figure A.4: Stress-strain curves from all the fracture test experiments performed with the PRP samples.

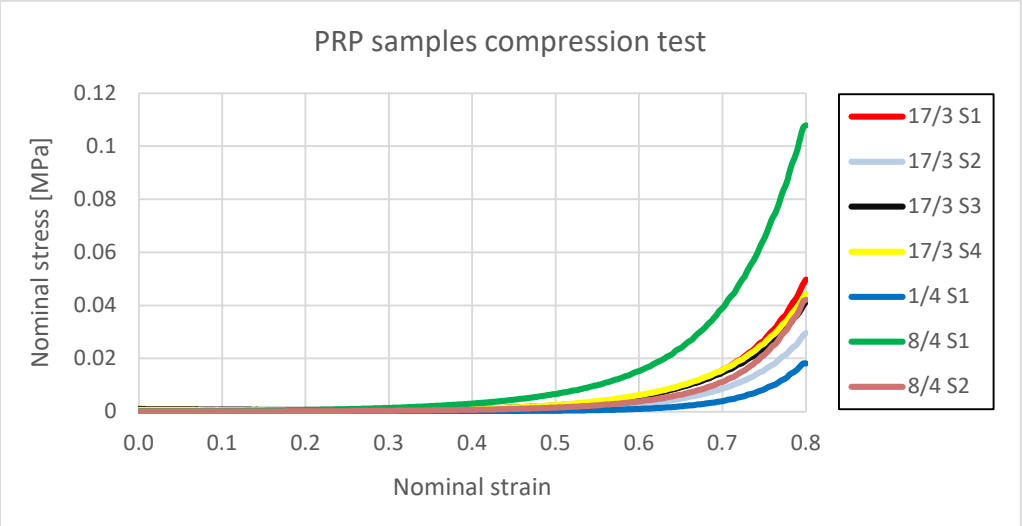

Figure A.5: Stress-strain curves from all the compression test experiments performed with the PRP samples.

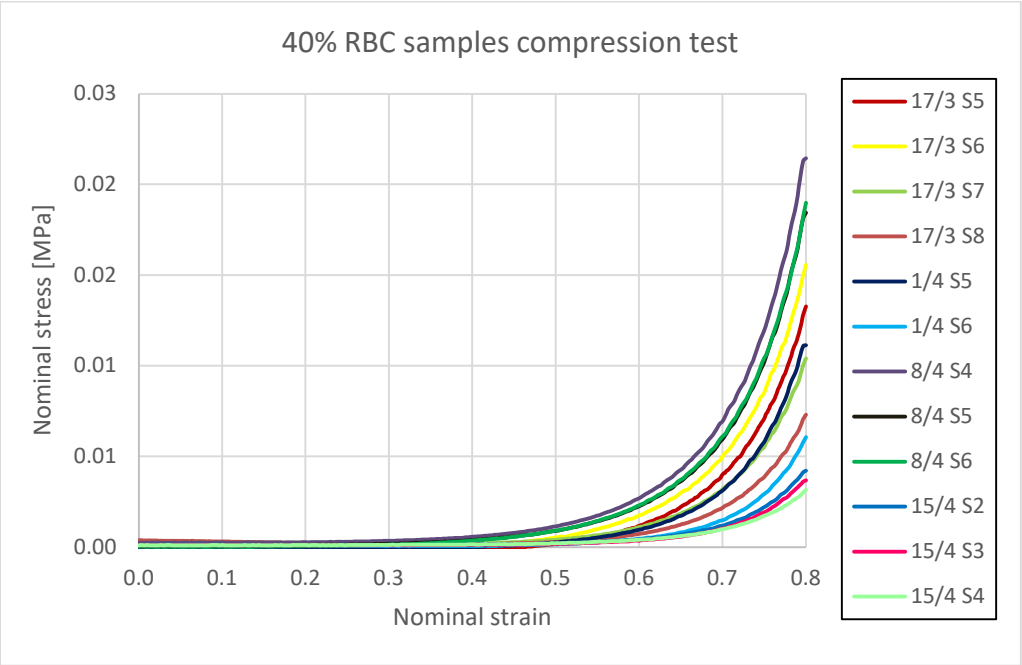

Figure A.6: Stress-strain curves from all the compression test experiments performed with the 40% RBC samples.

Appendix B: Filtering and extension stress-strain curve

```
clc;
clear all;

%This script is written to filter the stress-strain curves.
%In this example, the fracture models are filtered and extended to study the tensile
behavior of the clot analogs without damage.

%% PRP
A = {readtable('StressStrain_PRP_hole_224.txt')};

strain = A{:,1}{:,1};
stress = A{:,1}{:,2};

x = strain-strain(30);
y = stress-stress(30);
yy = spline(x,y);

strain_1 = linspace(0,max(x),50);
stress_1 = ppval(strain_1,yy);

stepsize_x = max(x)/49;
stepsize_y = max(y)/49;

extend_x = [strain_1(50):stepsize_x:(strain_1(50)+(20*stepsize_x))];
extend_y = [stress_1(50):stepsize_y:(stress_1(50)+(20*stepsize_y))];

new_strain = [strain_1, extend_x];
new_stress = [stress_1, extend_y];

figure(1)
plot(x(30:2018),y(30:2018),'o')
hold on
plot(strain_1,stress_1,'-')

figure(2)
plot(strain_1,stress_1,'k', 'LineWidth', 1.5)
hold on
plot(extend_x,extend_y,'r', 'LineWidth', 1.5)
xlabel('Nominal strain')
ylabel('Nominal stress [MPa]')
title('Extended stress-strain curve PRP sample')

figure(3)
plot(new_strain,new_stress)
xlabel('Strain')
ylabel('Stress [MPa]')

x_PRP = strain_1;
y_PRP = stress_1;
xy_PRP = [x_PRP(:),y_PRP(:)];
dlmwrite('StressStrain_PRP_hole_filtered.txt', xy_PRP, 'delimiter', ' ');

x_PRP_new = new_strain;
y_PRP_new = new_stress;
xy_PRP_new = [x_PRP_new(:),y_PRP_new(:)];
dlmwrite('StressStrain_PRP_hole_filtered_longer.txt', xy_PRP_new, 'delimiter', ' ');
```

```
%% RBC

A = {readtable('StressStrain_RBC_hole_224.txt')};

strain = A{:,1}{:,1};
stress = A{:,1}{:,2};

x = strain-strain(10);
y = stress-stress(10);
yy = spline(x,y);

strain_1 = linspace(0,max(x),50);
stress_1 = ppval(strain_1,yy);

stepsize_x = max(x)/49;
stepsize_y = max(y)/49;

extend_x = [strain_1(50):stepsize_x:(strain_1(50)+(20*stepsize_x))];
extend_y = [stress_1(50):stepsize_y:(stress_1(50)+(20*stepsize_y))];

new_strain = [strain_1, extend_x];
new_stress = [stress_1, extend_y];

figure(1)
plot(x,y,'o')
hold on
plot(strain_1,stress_1,'-')

figure(2)
plot(strain_1,stress_1,'k', 'LineWidth', 1.5)
hold on
plot(extend_x,extend_y,'r', 'LineWidth', 1.5)
xlabel('Nominal strain')
ylabel('Nominal stress [MPa]')
title('Extended stress-strain curve PRP sample')

figure(3)
plot(new_strain,new_stress)
xlabel('Strain')
ylabel('Stress [MPa]')

x_RBC = strain_1;
y_RBC = stress_1;
xy_RBC = [x_RBC(:),y_RBC(:)];
dlmwrite('StressStrain_RBC_hole_filtered_1.txt', xy_RBC, 'delimiter', ' ');

x_RBC_new = new_strain;
y_RBC_new = new_stress;
xy_RBC_new = [x_RBC_new(:),y_RBC_new(:)];
dlmwrite('StressStrain_RBC_hole_filtered_longer.txt', xy_RBC_new, 'delimiter', ' ');
```

Appendix C: Script empirical curve fitting MM295

Empirical curve fitting to obtain the material parameters for MM295 is performed using a MATLAB script that assumes that the material is incompressible. The MATLAB script is provided by Politecnico di Milano in Milan. The Yeoh model is selected to describe the non-linear behavior of the clot analogs during compression and tension.

```
% Empirical curve fitting
% This script fits a strain energy function of the form:
%    W = C10(I1-3)+C01(I2-3)+C20(I1-3)^2+C30(I1-3)^3+D1[exp(D2(I1-3))-1]
% Output is the stress-stretch curve plus corresponding parameter values.
% Parameters will be used in MM295.
%
% Ifit(1) -> C10
% Ifit(2) -> C01
% Ifit(3) -> C20
% Ifit(4) -> C30
% Ifit(5) -> D1
% Ifit(6) -> D2
clear;
clc;
close all;

Ifit = [1 0 1 1 0 0]; %Select the parameters needed for each model

%data = load('Stress-strain_compression_PRP_negative.txt');
data = load('Stress-strain_compression_RBC_negative.txt');
data(:,1) = data(:,1)+1

%%%%%%%%%%
Stress_Type = 'PK';
print_Fit2Do(Stress_Type,Ifit);
X0fit = [0.1 0.1 0 0 0 0];
nvar = sum(Ifit);
x0 = X0fit(Ifit>0);
LB = zeros(1,nvar);
UB = 1.0e8*ones(1,nvar);

options = optimset('LargeScale','off','Display','none','MaxFunEvals',5000,...
    'TolX',1e-12,'TolFun',1e-12,'TolCon',1e-12,'DiffMaxChange',0.5,...
    'DiffMinChange',1e-12);

[x, fval, exitflag, output] = fmincon(@(x) obj_fun(x,data,Ifit,Stress_Type),...
    x0,[],[],[],[],LB,UB,[],options);

print_optout(exitflag,output);
print_output(x,Ifit,Stress_Type,data);

function F = obj_fun(x,data,Ifit,Stress_Type)
%
%
 sig = stress(x,data(:,1),Ifit,Stress_Type);
 F = sum((data(:,2)-sig).^2);
end

function sig = stress(x,lam,Ifit,Stress_Type)
%
coef = 1.0*Ifit;
```

```
coef(Ifit>0) = x;
C10 = coef(1);
C01 = coef(2);
C20 = coef(3);
C30 = coef(4);
D1  = coef(5);
D2  = coef(6);
I1 = lam.^2 + 2./lam;
I2 = 0.5*(I1.^2-lam.^4-2./(lam.^2));
W1 = C10+2.0*C20*(I1-3.0)+3.0*C30*(I1-3.0).^2+D1*D2*exp(D2*(I1-3.0));
W2 = C01;

%
% By default PK stress tensor is calculated
%
dI1dlam = lam-1./(lam.^2.0);
dI2dlam = I1.*dI1dlam - (lam.^3.0 - 1./(lam.^3.0));
PK = 2.0*W1.*dI1dlam + 2.0*W2.*dI2dlam;
switch Stress_Type
   case 'PK2'
      sig = PK./lam;
   case 'PK'
      sig = PK;
   case 'Cauchy'
      sig = PK.*lam;
end
end

function print_Fit2Do(Stress_Type,Ifit)
%
%
switch Stress_Type
   case 'PK2'
      fprintf('Fitting Second Piola Kirchhoff stress data\n');
   case 'PK'
      fprintf('Fitting First Piola Kirchhoff stress data\n');
   case 'Cauchy'
      fprintf('Fitting Cauchy stress data\n');
end
fprintf('Fitting the following constants of the Strain Energy Function:\n');
fprintf('W = C10(I1-3)+C01(I2-3)+C20(I1-3)^2+C30(I1-3)^3+D1[exp(D2(I1-3))-1]\n');
if(Ifit(1)==1) fprintf('C10\n'); end
if(Ifit(2)==1) fprintf('C01\n'); end
if(Ifit(3)==1) fprintf('C20\n'); end
if(Ifit(4)==1) fprintf('C30\n'); end
if(Ifit(5)==1) fprintf(' D1\n'); end
if(Ifit(6)==1) fprintf(' D2\n'); end
end

function print_output(x,Ifit,Stress_Type,data)
%
%
coef = 1.0*Ifit;
coef(Ifit>0) = x;
fprintf('Identified Parameters:\n');
if(Ifit(1)==1) fprintf('C10: %f\n',coef(1)); end
if(Ifit(2)==1) fprintf('C01: %f\n',coef(2)); end
if(Ifit(3)==1) fprintf('C20: %f\n',coef(3)); end
if(Ifit(4)==1) fprintf('C30: %f\n',coef(4)); end
```

```
if(Ifit(5)==1) fprintf(' D1: %f\n',coef(5)); end
if(Ifit(6)==1) fprintf(' D2: %f\n',coef(6)); end
fp=fopen('fit_results.dat','w');
fprintf(fp,'%%C10 C01 C20 C30 D1 D2\n');
fprintf(fp,'%f coef\n');
fclose(fp);
sig = stress(x,data(:,1),Ifit,Stress_Type);
plot(data(:,1),data(:,2),'LineWidth',3); hold
plot(data(:,1),sig,'LineWidth',3);
xlabel('Stretch','FontSize',18);
switch Stress_Type
   case 'PK2'
      ylabel('PK2 stress','FontSize',18);
   case 'PK'
      ylabel('PK stress','FontSize',18);
   case 'Cauchy'
      ylabel('Cauchy stress','FontSize',18);
end
grid on;
legend('Experiment','Yeoh');
title('Stress-stretch PRP compression experiment and Yeoh model')
end

function print_optout(exitflag,output)
%
%
%
switch exitflag
   case -1
      fprintf('Stopped by an output function or plot function\n');
   case -2
      fprintf('No feasible point was found.\n');
   case -3
      fprintf('Interior Point, sqp-legacy and sqp algorithm.\n');
      fprintf('Objective function at current iteration went below \n');
      fprintf('options.ObjectiveLimit and maximum constraint violation \n');
      fprintf('was less than options.ConstraintTolerance\n');
   case 0
      fprintf('Max. number of iterations or Max. number of function evaluations\n');
      fprintf('excedeed. Increase MaxFunEvals and/or MaxIter and rerun\n');
   case 1
      fprintf('First-order optimality measure was less than options.\n');
      fprintf('OptimalityTolerance, and maximum constraint violation \n');
      fprintf('was less than options.ConstraintTolerance\n');
   case 2
      fprintf('Algorithm active-set. Change in x was less than options.\n');
      fprintf('StepTolerance and maximum constraint violation was less \n');
      fprintf('than options.ConstraintTolerance.\n');
   case 3
      fprintf('Trust-region-reflective algorithm. Change in the objective\n');
      fprintf('function value was less than options.FunctionTolerance \n');
      funtion('and maximum constraint violation was less than
options.ConstraintTolerance.\n');
   case 4
      fprintf('Algorithm active-set. Magnitude of the search direction was\n');
      fprintf('less than 2*options.StepTolerance and maximum constraint \n');
      fprintf('violation was less than options.ConstraintTolerance.\n');
   case 5
      fprintf('Algorithm active-set. Magnitude of directional derivative \n');
```

```
        fprintf('in search direction was less than 2*options.OptimalityTolerance \n');
        fprintf('and maximum constraint violation was less than \n');
        fprintf('options.ConstraintTolerance.\n');
end
fprintf('\nStatistics of the Optimization\n');
fprintf('Number of Iterations          : %d\n',output.iterations);
fprintf('Number of Function Evaluations: %d\n',output.funcCount);
fprintf('First Order Optimality        : %f\n',output.firstorderopt);
fprintf('%s\n',output.message);
end
```

Appendix D: Numerical keywords cube model

In this appendix, the code is added for **the compression test using the cube model with the PRP sample and MM181 PR = 0.30,** as used in chapter 4. The stress-strain curve of the PRP sample and the node set is reduced to create a compact appendix. An explanation of the numerical keywords used in the cube model is presented after the code.

```
$# LS-DYNA Keyword file created by LS-PrePost(R) V4.8.11 - 22Feb2021
*KEYWORD
*TITLE
$#                                                                title
LS-DYNA keyword deck by LS-PrePost
*CONTROL_ENERGY
$#    hgen      rwen    slnten     rylen     irgen
         2         2         2         2         2
*CONTROL_OUTPUT
$#   npopt    neecho    nrefup    iaccop     opifs    ipnint    ikedit    iflush
       0         0         0         0       0.0         0       100      5000
$#   iprtf    ierode   tet10s8    msgmax    ipcurv      gmdt   ip1dblt      eocs
       0         0         2        50         0       0.0         0         0
$#   tolev    newleg    frfreq     minfo    solsig    msgflg    cdetol
       2         0         1         0         0         0      10.0
$# phschng    demden   icrfile   spc2bnd    penout    shlsig   hisnout    engout
       0         0         0         0         0         0         0         0
$#    insf    isolsf      ibsf      issf    mlkbag
       0         0         0         0         0
*CONTROL_TERMINATION
$#  endtim    endcyc     dtmin    endeng    endmas     nosol
     100.0         0       0.0       0.0  1.000000E8         0
*CONTROL_TIMESTEP
$#  dtinit    tssfac      isdo    tslimt     dt2ms      lctm     erode     ms1st
      0.0       0.8         0       0.0       0.0         0         0         0
$#  dt2msf   dt2mslc     imscl    unused    unused     rmscl    unused      ihdo
       0.0         0         0                             0.0                 0
*DATABASE_GLSTAT
$#      dt    binary      lcur     ioopt
       5.0         0         0         1
*DATABASE_MATSUM
$#      dt    binary      lcur     ioopt
       5.0         0         0         1
*DATABASE_NODFOR
$#      dt    binary      lcur     ioopt
       5.0         0         0         1
*DATABASE_BINARY_D3PLOT
$#      dt      lcdt      beam     npltc    psetid
       5.0         0         0         0         0
$#   ioopt      rate    cutoff    window      type      pset
       0       0.0       0.0       0.0         0         0
*DATABASE_EXTENT_BINARY
$#   neiph     neips    maxint    strflg    sigflg    epsflg    rltflg    engflg
       0         0         3         1         1         1         1         1
$#  cmpflg    ieverp    beamip     dcomp      shge     stssz    n3thdt   ialemat
```

```
        0          0          0          1          2          3          2          1
$# nintsld   pkp_sen      sclp     hydro     msscl     therm    intout    nodout
        0          0        1.0         0         0         0
$#    dtdt    resplt     neipb     quadr     cubic
       0         0         0         0         0
*BOUNDARY_PRESCRIBED_MOTION_SET
$#     nsid       dof       vad      lcid        sf       vid     death           birth
         1         2         2         1      -0.8         0  1.00000E28       0.0
*BOUNDARY_SPC_NODE
$#      nid       cid      dofx      dofy      dofz     dofrx     dofry     dofrz
         1         0         1         1         1         0         0         0
*PART
$#      title boxsolid
$#      pid     secid       mid     eosid      hgid      grav    adpopt      tmid
         1         1         1         0         1         0         0         0
*SECTION_SOLID
$#   secid    elform       aet    unused    unused    unused    cohoff    unused
         1         1         0                                        0
*MAT_SIMPLIFIED_RUBBER/FOAM_TITLE
PRP
$#      mid        ro        km        mu         g      sigf       ref     prten
         1     0.001       0.5      0.05       0.0       0.0       0.0       0.0
$#      sgl        sw        st   lc/tbid   tension     rtype    avgopt   pr/beta
        1.0       1.0       1.0         2      -1.0       0.0       0.0       0.3
$#   lcunld        hu     shape      stol     visco    hisout
         0         1.0       0.0         0       0.0       0.0
*HOURGLASS
$#     hgid       ihq        qm       ibq        q1        q2    qb/vdc        qw
       1          6        1.0         0       1.5      0.06       1.0       1.0
*DEFINE_CURVE_TITLE
One
$#     lcid      sidr       sfa       sfo      offa      offo    dattyp     lcint
       1         0       1.0       1.0       0.0       0.0         0         0
$#               a1                  o1
              0.0                 1.0
           1000.0                 1.0
*DEFINE_CURVE_TITLE
Displacement
$#     lcid      sidr       sfa       sfo      offa      offo    dattyp     lcint
         1         0       1.0       1.0       0.0       0.0         0         0
$#               a1                  o1
              0.0                 0.0
            100.0                 1.0
           1000.0                 1.0
*DEFINE_CURVE_TITLE
PRP
$#     lcid      sidr       sfa       sfo      offa      offo    dattyp     lcint
       10         0        1 .0      1.0       0.0       0.0         0         0
$#               a1                  o1
             -0.8                -0.04215
```

```
*DAMPING_PART_MASS
$#     pid      lcid        sf      flag
       1         1         1.0         0
*ELEMENT_SOLID
$#   eid     pid      n1      n2      n3      n4      n5      n6      n7      n8
       1       1       1       2       4       3       5       6       8       7
*NODE
$#   nid             x             y             z      tc      rc
     1           0.0           0.0           0.0       0       0
     2           1.0           0.0           0.0       0       0
     3           0.0           1.0           0.0       0       0
     4           1.0           1.0           0.0       0       0
     5           0.0           0.0           1.0       0       0
     6           1.0           0.0           1.0       0       0
     7           0.0           1.0           1.0       0       0
     8           1.0           1.0           1.0       0       0
*SET_NODE_LIST_TITLE
Compression
$#     sid       da1       da2       da3       da4    solver
       1         0.0       0.0       0.0       0.0     MECH
$#    nid1      nid2      nid3      nid4      nid5      nid6      nid7      nid8
       7         3         4         8         0         0         0         0
*END
```

Numerical keywords explanation

The keywords used in the cube model can be subdivided into several categories. Each category will be explained briefly, apart from *MAT, *ELEMENT, *NODE, and *SET.

***CONTROL**

A total of four control keywords are implemented in the model. CONTROL_ENERGY is added to provide information about the energy dissipation. CONTROL_OUTPUT is used to set the diverse output parameters, but it does not control the information (see DATABASE_EXTENT_BINARY). From a sensitivity analysis, it could be concluded that it was not necessary to apply a very little timestep or increase the termination time. The termination time is defined in the keyword CONTROL_TERMINATION, with a termination time of 100 ms. The timestep is set to the default value in the keyword CONTROL_TIMESTEP. The scale factor for computed time step (TSSFAC) is set to 0.8 to improve the stability of the model.

***DATABASE**

To select the output necessary for post-processing analysis, the keyword ASCII_OPTION is added. Here the global data (GLSTAT), material energies (MATSUM), and nodal force groups (NODFOR) are selected to obtain all output values necessary for post-processing. To collect the curves from the simulation, the BINARY_3D_PLOT is also included as a keyword. DATABASE_EXTENT_BINARY is used to control the content of the binary output database d3plot.

***BOUNDARY**

Nodes need to be identified to apply boundary conditions on the specific nodes. Single point constraint is used to apply translational constraints on each node (BOUNDARY_SPC_SET). Displacement is applied in the y-translational direction to the upper nodes of the cube, using a prescribed motion boundary condition (BOUNDARY_PRESCRIBED_MOTION).

***PART**

The keyword PART includes the section, material properties, and hourglass control that are assigned to the part.

***SECTION**

The reduced element formulation is used by setting ELFORM to a value of 1. This element formulation is efficient and accurate but needs hourglass stabilization. The keyword HOURGLASS is added to provide this stabilization.

***HOURGLASS**

Hourglass type 6 control can be used in 2D and 3D solid elements. As recommended for foam materials, the hourglass coefficient (QM) value is set to 1. All other settings are set to the default settings.

***DEFINE**

Two different curves are defined that will be used as input for other keywords. The application of tension or compression is done by defining a displacement curve. These curves differ for each test. The uniaxial test data necessary for MM181 to define the material properties is also imported as a curve.

***DAMPING**

Damping has been added to the model by adding the keyword PART_MASS. From a sensitivity analysis, it could be concluded that applying a very large damping was unnecessary.

Appendix E: Differences cube and geometry model

In this appendix, the keyword differences between the cube model and geometry model will be discussed briefly.

***SET**
To apply boundary conditions, it was necessary to make two different node sets in the geometry models. One node set contains the bottom nodes and one the upper nodes.

***CONTROL**
A termination time of 200 ms has been used in the geometry models.

***DATABASE**
The resultant nodal force of the fixed bottom nodes was used to calculate the nominal stress and strain. Therefore the keyword NODAL_FORCE_GROUP was added.